Physics of Fluids

Aspect ratio studies on insect wings

Cite as: Phys. Fluids **31**, 121301 (2019); https://doi.org/10.1063/1.5129191
Submitted: 26 September 2019 . Accepted: 21 November 2019 . Published Online: 19 December 2019

S. S. Bhat, J. Zhao (赵季生), J. Sheridan, K. Hourigan, and M. C. Thompson

COLLECTIONS

This paper was selected as Featured

View Online Export Citation CrossMark

AIP Conference Proceedings
FLASH WINTER SALE!
50% OFF ALL PRINT PROCEEDINGS
ENTER CODE 50DEC19 AT CHECKOUT

AIP Publishing

© 2019 Author(s).

Physics of Fluids REVIEW scitation.org/journal/phf

Aspect ratio studies on insect wings

Cite as: Phys. Fluids 31, 121301 (2019); doi: 10.1063/1.5129191
Submitted: 26 September 2019 • Accepted: 21 November 2019 •
Published Online: 19 December 2019

View Online Export Citation CrossMark

S. S. Bhat, J. Zhao (赵季生), J. Sheridan, K. Hourigan, and M. C. Thompson[a)]

AFFILIATIONS

Fluids Laboratory for Aeronautical and Industrial Research (FLAIR), Department of Mechanical and Aerospace Engineering, Monash University, Melbourne, VIC 3800, Australia

[a)]Electronic mail: mark.thompson@monash.edu

ABSTRACT

The wing aspect ratio ($\mathcal{AR}$), that is, the ratio of the wingspan to the mean wing chord, is the most important geometrical parameter describing an insect wing. While studies have shown that a change in $\mathcal{AR}$ affects the flow structure as well as the aerodynamic force components on wings, the reasons behind the wide variety of aspect ratios observed in nature remain underexplored. Further to this, motivated by the developments in micro-air vehicles (MAVs), determining an optimum $\mathcal{AR}$ is important for their efficient operation. While the effects on flow structure appear to be, at least superficially, broadly consistent across different studies, the effects on aerodynamic forces have been more strongly debated. Indeed, the considerable variation of force coefficients with $\mathcal{AR}$ in different studies suggests different optimal $\mathcal{AR}$s. To help explain this, recent studies have pointed out the coupled effects of $\mathcal{AR}$ with other parameters. Specifically, the use of Reynolds and Rossby numbers based on alternative scalings helps to at least partially decouple the effects of $\mathcal{AR}$ and also to reconcile previous conflicting trends. This brief review presents an overview of previous studies on aspect-ratio effects of insectlike wings summarizing the main findings. The suggested alternative scalings of Reynolds and Rossby numbers, using the wingspan as the characteristic length, may be useful in aiding the selection of the optimal aspect ratios for MAVs in the future.

Published under license by AIP Publishing. https://doi.org/10.1063/1.5129191

I. INTRODUCTION

Flying is a way of life for the majority of animals, including birds, bats, and insects. The survival and continuing evolution of these animals depend on their flight performance. Motivated by research into aircraft, the aerodynamics of large flying animals has been studied in detail over the past several decades. However, the aerodynamics of their smaller counterparts is, perhaps, less well understood. Recent developments in the design of micro-air vehicles (MAVs) have resulted in a growing interest in the study of the insect wing aerodynamics. Various morphological as well as kinematic parameters of flapping wings have been studied by researchers in the past few years.[1–10]

In general, insect wings are morphologically different from those of birds. Bird wings are observed to have sharp tips, whereas insect wings have a smooth transition of the wing's leading edge into the wing tip along a curve. Birds mostly generate lift in the downstroke of the wing, whereas insects generate lift in both upstroke and downstroke. Of course, as has been noted by Azevedo *et al.*[11] and Wootton,[12] not all morphological parameters are related to insect locomotion. Some are related to wing-folding and thermoregulation as well. However, wing morphology is important in determining the aerodynamic performance of wings of insects and of insect-inspired MAVs. The key morphological feature of a wing is its aspect ratio, given by

$$\mathcal{AR} = \frac{b}{\bar{c}}, \tag{1}$$

where b is the wingspan and $\bar{c}$ is the mean wing-chord, as shown in the schematic in Fig. 1. The mean chord is calculated as the ratio of the wing area (S) to the wingspan (b).

When scaled with the mean chord, wings with higher values of $\mathcal{AR}$ result in a larger wing area (S) than that from small-$\mathcal{AR}$ wings. This affects the mean lift generated by the wing in a flapping cycle as indicated by blade element theory, $L = C_L \rho U_g^2 S/2$, where C_L is the lift coefficient of the wing, ρ is the density of the surrounding medium, and U_g is the mean flapping velocity at the radius of gyration. However, the mean lift is also affected by wing flapping speeds, depending on the wing Reynolds number $Re = U_g \bar{c}/\nu$,[13–15] where ν is the viscosity of the surrounding medium. Moreover, a high-$\mathcal{AR}$ wing has a larger radius of gyration (R_g) scaled with the mean chord. This ratio, in the context

Published under license by AIP Publishing

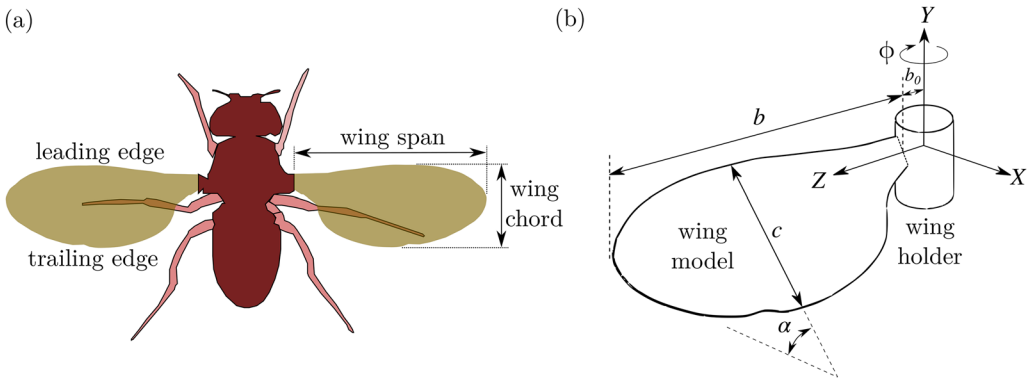

FIG. 1. Schematic of (a) a fruit fly and its wing characteristics and (b) a wing model used in experimental studies.

of insectlike wings, is known as the Rossby number ($Ro = R_g/\bar{c} = \mathcal{A}R_g/b$).[16–19] As a result, the lift acting on the wing can be expressed as

$$L = C_L \frac{1}{2}\rho v^2 Re^2 \mathcal{A} = C_L \frac{1}{2}\rho \dot{\phi}^2 S^2 \frac{Ro^2}{\mathcal{A}}, \tag{2}$$

where $\dot{\phi}$ is the angular velocity of flapping. Therefore, the effects of $\mathcal{A}$ on the wing aerodynamics are coupled with the effects of Re and Ro.[20,21]

The detailed effects of $\mathcal{A}$ on the wing aerodynamics have been debated over the past few decades. Seemingly inconsistent results from various experimental studies[20,22–31] pose several questions: How does the $\mathcal{A}$ affect the flow characteristics over a wing? What is an optimized $\mathcal{A}$? Does the value of the optimized $\mathcal{A}$ change with the flapping speed? Why is there a wide range of $\mathcal{A}$ observed in nature? This review discusses these issues and, where possible, presents some possible answers based on recent research results. Motivated by our recent study,[32] seemingly contradictory previous studies are reconciled using the span-based scaling of Re and Ro.

In this review, first, a summary of various aspect ratios observed in nature and their relation with Re and Ro is discussed. Furthermore, the results from various aspect-ratio studies are categorized into two groups, namely, those showing the effects on the flow structure and others showing the effects on the aerodynamic forces. This detailed discussion is necessary to document important previous studies and to show how they relate to each other. Furthermore, a polynomial model has been developed to predict the lift coefficients for various $\mathcal{A}$-Re-Ro combinations, which shows that the proposed span-based scaling indeed helps reconcile the apparently conflicting trends in previous studies.

II. ASPECT RATIOS FOUND IN NATURE AND MAVs

Since insect wings have various shapes, the direct measurement of the mean chord, $\bar{c}$, may not be possible in each case. Therefore, $\mathcal{A}$ is also often alternatively defined as a relation between two measurable quantities, namely, the wingspan b and the wing area S,[22,33,34] such that

$$\mathcal{A} = \frac{b^2}{S}. \tag{3}$$

The wingspan and wing area can be measured, for example, by filming insect wings.[35,36] In some studies, for example, by Usherwood and Ellington,[22] $\mathcal{A}$ has been defined as $4b^2/S'$, where S' is the total area of two wings. For the purpose of comparison, all the $\mathcal{A}$ values in Appendix A have been scaled according to Eq. (3).

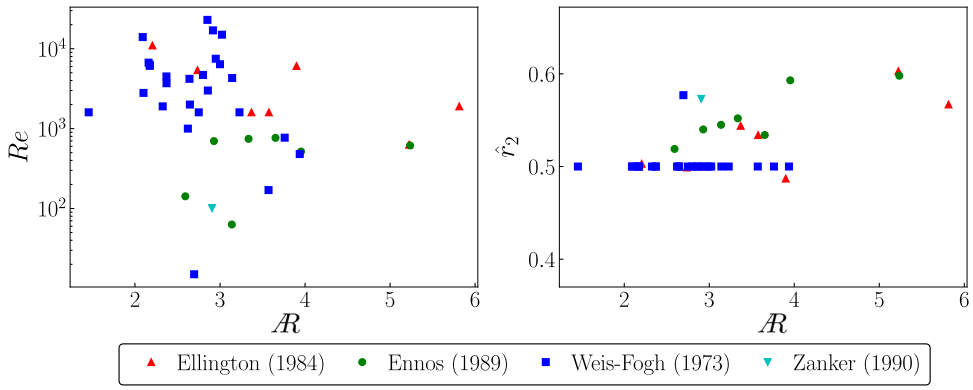

FIG. 2. Data of $\mathcal{A}$, Re, and $\hat{r}_2$ of various insect wings obtained from the work of Weis-Fogh,[4] Ellington,[35] Ennos,[41] and Zanker.[46] Weis-Fogh has assumed most wings to be semielliptic in shape; thus, having $\hat{r}_2 = 0.5$. Details can be found in Appendix B.

Published under license by AIP Publishing

Interestingly, birds and bats are found to enhance the lift on their wings by dynamically changing the wingspan during their flapping motion.[37,38] Unlike insects, birds have bones in their wings, which enable them to change their wingspan, thereby changing the aspect ratio dynamically. This change in the wingspan results in changes in the instantaneous flow structure and in the overall flight performance.[39] In general, insect wings have aspect ratios in the range $1.5 \leq \mathcal{AR} \leq 6$, whereas bird wings have those in the range $5.5 \leq \mathcal{AR} \leq 19$ (see the data by Tennekes[40]). In comparison with insects, the longer wingspans of birds and bats help in providing a larger wing area, allowing them to glide while maintaining low angles of attack. However, insect wings have a lower $\mathcal{AR}$ as compared to that of birds, owing to the wingspan being limited by their small body lengths (see the work of Ellington[35]). With a reduction in $\mathcal{AR}$, the induced drag increases.[41] Simultaneously, the ratio of lift to drag (L/D), also known as the glide ratio, decreases. Thus, low L/D ratios cause gliding to be not feasible in the case of insects, requiring them to flap their wings to maintain flight. In fact, the

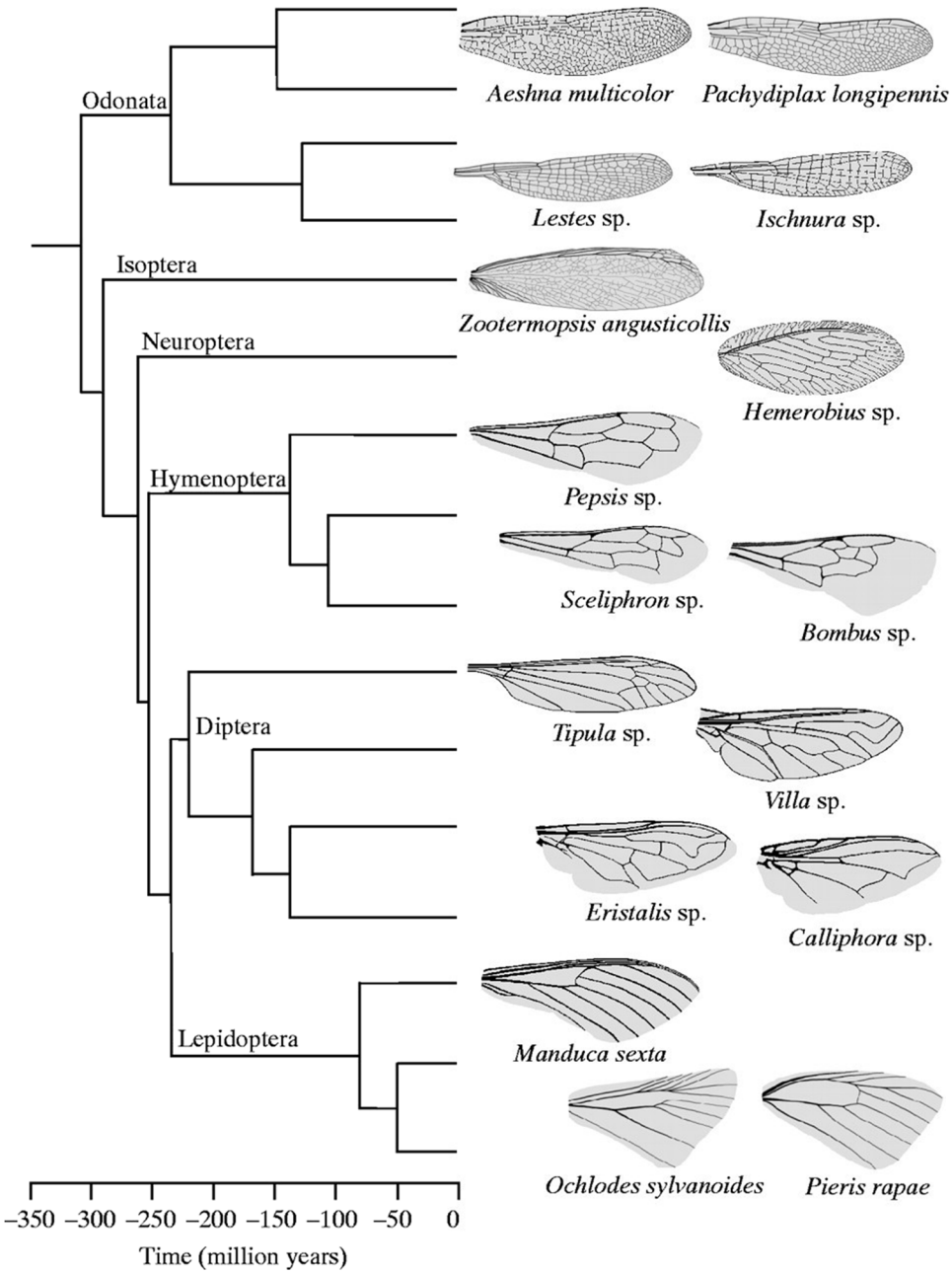

FIG. 3. Various wing planforms, as given by Combes and Daniel.[47] Figure republished with permission from A. Combes and T. L. Daniel, "Flexural stiffness in insect wings I. Scaling and the influence of wing venation," J. Exp. Biol. **206**, 2979 (2003). Copyright 2003 Company of Biologists Ltd.

Published under license by AIP Publishing

wing-beat rate in animals is observed to increase nearly exponentially with a decrease in wingspan.[42] Consequently, smaller insects are observed to have low-$\mathcal{AR}$ wings with a high wing-beat frequency. Some large insects, such as butterflies, locusts, and dragonflies, can use both gliding and flapping motions intermittently.[43,44] However, their gliding speeds are limited by their inability to alter the wingspan.[45]

The wing Reynolds number, Re, depends on the wing size and the wing-beat frequency. In this case, Re is generally defined by

$$Re = \frac{U_g \bar{c}}{\nu}. \tag{4}$$

For the wing flapping with a sweep amplitude ϕ_A at the rate of n Hz, the mean velocity U_g is calculated as $4\phi_A n R_g$. The term *sweep*, in this case, refers to the rotation of the wing about the axis normal to the stroke plane, shown as ϕ in Fig. 1(b). This motion is also called the *translation* in many studies.[13,16,21] Even though the range of Re for various insects is large ($10^2 < Re < 10^4$), the range of $\mathcal{AR}$ is observed to be typically within $2 < \mathcal{AR} < 7.5$, as can be seen in Fig. 2. Many insect wings can be reasonably approximated by semielliptic shapes;[4] however, some *Hymenoptera* and *Lepidoptera* species are better approximated by triangular shapes. The range of wing shapes can be seen in Fig. 3.

Ellington[35] has derived *laws of wing shapes* to which most wings adhere. According to these laws, the normalized radii of the second and third moments of area of a wing, i.e., $\hat{r}_2(S)$ and $\hat{r}_3(S)$, are related to the centroid of the wing area $\hat{r}_1(S)$ such that $\hat{r}_2(S) = 0.929[\hat{r}_1(S)]^{0.732}$ and $\hat{r}_3(S) = 0.9[\hat{r}_1(S)]^{0.581}$. Here, the normalized radius of a wing's kth moment of area is given by

$$\hat{r}_k^k(S) = \int_0^1 \hat{c}\hat{r}^k \mathrm{d}\hat{r}, \tag{5}$$

where $\hat{c}$ is the local wing chord normalized by $\bar{c}$ and $\hat{r}$ is the spanwise distance normalized by the wingspan (b). Broadly, either $\hat{r}_1$ or $\hat{r}_2$, in addition to $\mathcal{AR}$, might be sufficient to reconstruct an approximate wing planform using a *Beta function* approximation, as shown by Ellington.[35] Data for various insects obtained from the literature show that $\hat{r}_2$ varies in a very narrow range, $0.5 < \hat{r}_2 < 0.6$, as can be seen in Fig. 2.

III. EFFECTS OF $\mathcal{AR}$ ON THE WING AERODYNAMICS

Insight into the influence of $\mathcal{AR}$ on the wing aerodynamics can be gained by noting the relation between $\mathcal{AR}$ and various acceleration terms in the Navier-Stokes equations. The nondimensionalized Navier-Stokes equations in a noninertial rotating frame of reference for a flapping wing have been derived by Lentink and Dickinson[48] as

$$\frac{D\boldsymbol{u}}{Dt} + \frac{1}{J^2+1}\left[\frac{1}{A^*}\dot{\boldsymbol{\Omega}} \times \boldsymbol{r} + \frac{1}{\mathcal{AR}}\boldsymbol{\Omega} \times (\boldsymbol{\Omega} \times \boldsymbol{r}) + \frac{1}{\mathcal{AR}} 2\boldsymbol{\Omega} \times \boldsymbol{u}\right] = -\nabla p + \frac{1}{Re}\nabla^2 \boldsymbol{u}, \tag{6}$$

where $\boldsymbol{r}$, $\boldsymbol{u}$, $\boldsymbol{\Omega}$, and $\dot{\boldsymbol{\Omega}}$ are the normalized displacement, velocity, angular velocity, and angular acceleration vectors, respectively; t and p represent the normalized time and pressure, respectively; and the nondimensional numbers J and A^* represent the advance ratio and the chord-lengths swept by the wing tip, respectively. In the case of a hovering insect wing, as is considered in most studies discussed in this review, $J = 0$. It should be noted that the velocity and length terms in this equation are normalized by the wing-tip velocity and the wing chord, respectively, following the proposed scalings of Lentink and Dickinson. Moreover, $\mathcal{AR}$ in Eq. (6) has been defined by Lentink and Dickinson as $R/\bar{c}$, which did not account for the wing-root offset.

It has been established that the centripetal and Coriolis forces are important for the stability of the leading edge vortex (LEV) responsible for a high lift force over an insect wing.[16,25,49,50] Equation (6) shows that the centripetal and Coriolis accelerations scale with $\mathcal{AR}$. Hence, this will affect the formation and stability of vortical structures over the wing. In view of this, several experimental and computational studies have investigated the effects of $\mathcal{AR}$ on both the vortical flow structures and the aerodynamic forces. Observations with respect to the influence on the flow structures are broadly similar; however, inconsistencies exist in the reported effects on aerodynamic forces, as described in Secs. III A–III E.

A. Effects on the flow structure

A flapping stroke of an insect can be divided into the forward and the backward half strokes. During the majority of each half stroke, the wing rotates about the vertical axis, which is called the sweep motion. Toward the end of a half stroke, the wing flips and changes its orientation, which is called the pitch motion. Insect wings flap at relatively low Reynolds numbers, maintaining high angles of attack ($\alpha \sim 45°$). A purely translating wing would stall at such angles with a loss of lift. However, in flapping insect wings, a high lift is maintained, which can be attributed to several unsteady mechanisms. Nevertheless, it has been widely accepted that the high lift over an insect wing is primarily obtained as a result of a stable attachment of the LEV.[5,51]

The LEV is formed from the shear layer separating from the leading edge during the sweep motion. The shear layer curls up on the wing suction side to form the LEV, which is conical in shape, growing in size from the wing root to the wing tip. LEVs have also been observed to be important in the hydrodynamics of the flapping motion of fish tails[52] and stingrays.[53] In insects, the LEV has been observed to be stabilized during the sweep motion by the action of the centripetal and Coriolis accelerations.[16,54,55] Since these important terms in Eq. (6) scale with $\mathcal{AR}$, the stability of the LEV must be dependent on $\mathcal{AR}$. This can ultimately affect the lift acting on the wing.

In their experiments on a rotating wing at Re = 13 000, Kruyt *et al.*[29] observed that the LEV remains attached up to the spanwise location $r/c < 4$. Further outboard, the LEV lifts away from the wing surface, as can be seen in Fig. 4. The proximity of the LEV to the surface for low $\mathcal{AR}$ results in a higher magnitude of the normalized suction pressure beneath the LEV. Kruyt *et al.* showed that the LEV circulatory lift coefficient (C_l) is higher at low $\mathcal{AR}$ and decreases steeply beyond $\mathcal{AR} > 4$. The flow over an $\mathcal{AR}$ = 10 wing largely resembles that over a purely translating wing, except in the inboard region (at $r/c < 4$), where the 3D effects are prominent. For locations beyond $r/c = 4$, the size of the LEV at that location is limited by the trailing edge and it will be similar for larger $\mathcal{AR}$.

Published under license by AIP Publishing

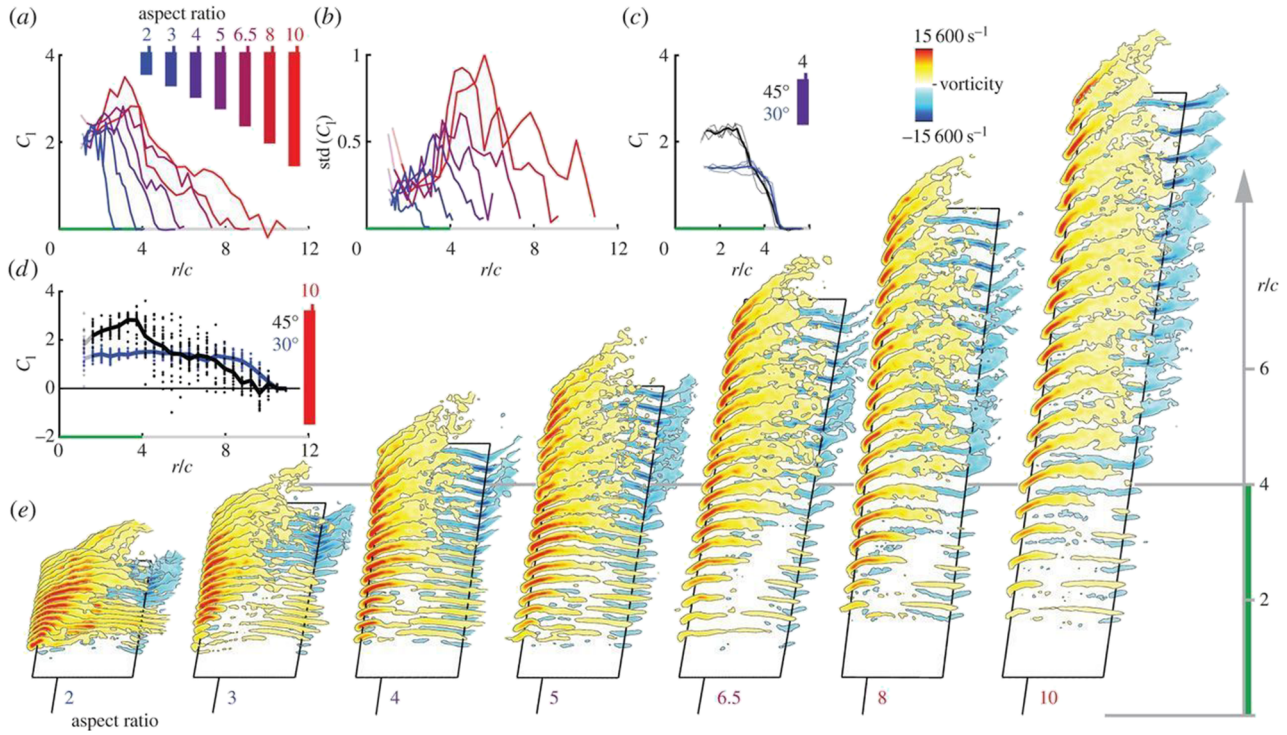

FIG. 4. The vorticity contours inside the LEV core at various spanwise sections are shown for various $\mathcal{AR}$. Republished with permission from Kruyt *et al.*, "Power reduction and the radial limit of stall delay in revolving wings of different aspect ratio," J. R. Soc., Interface **12**, 20150051 (2015). Copyright 2015 Royal Society.

At a specific spanwise location normalized by wingspan, the size of the LEV is observed to be different for different $\mathcal{AR}$, as has been observed by Luo and Sun.[23] For example, Fig. 5 shows that at location $r_a = r/b = 0.4$, the LEV size for $\mathcal{AR} = 2.8$ is smaller than that for a wing of $\mathcal{AR} = 5.5$. However, at location $r_b = r/b = 0.6$, the LEV for $\mathcal{AR} = 2.8$ is slightly larger, whereas that for $\mathcal{AR} = 5.5$ is split into two corotating vortices called the dual-LEVs. Here, the primary LEV at the leading edge is lifted away from the wing surface. It can be noted that the split may be caused by induced opposite-signed secondary vorticity that has developed between the two vortex cores, as has been discussed by Lu *et al.*[56] This secondary vorticity is developed as a result of the interaction of the two corotating LEVs with the wing surface. The secondary vortex (SV) is lifted away from the surface by the action of the larger LEV core, ultimately causing the LEV to split.

Han *et al.*[26] also observed that the LEV over a flapping wing is lifted away from the surface at a higher $\mathcal{AR}$. Figure 6 shows that the LEV over a wing of $\mathcal{AR} = 1.5$ is close to the wing surface, allowing the reattachment of separated flow beyond the midchord. However, for $\mathcal{AR} = 3$ and 6, the LEV is lifted off the wing surface and the separated

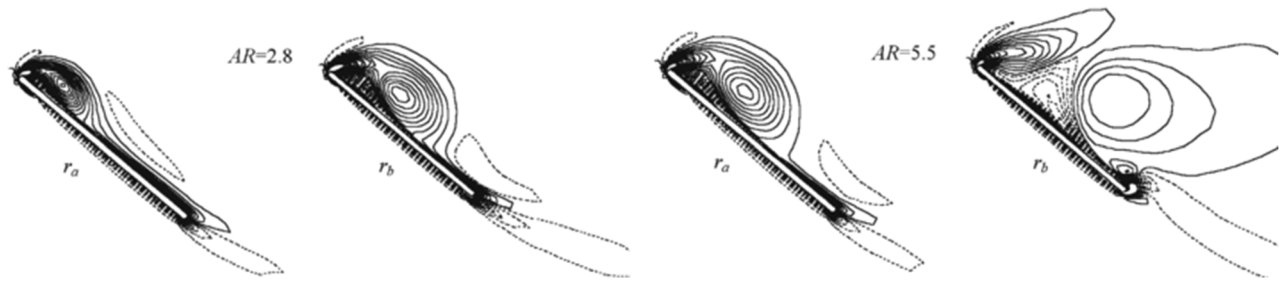

FIG. 5. Vorticity contours over a wing are shown at two different spanwise locations for $\mathcal{AR} = 2.8$ and $\mathcal{AR} = 5.5$. r_a and r_b represent the locations $r/b = 0.4$ and $r/b = 0.6$, respectively. Figure adapted with permission from G. Luo and M. Sun, "The effects of corrugation and wing planform on the aerodynamic force production of sweeping model insect wings," Acta Mech. Sin. **21**, 531–541 (2005). Copyright 2005 Springer Nature.

Published under license by AIP Publishing

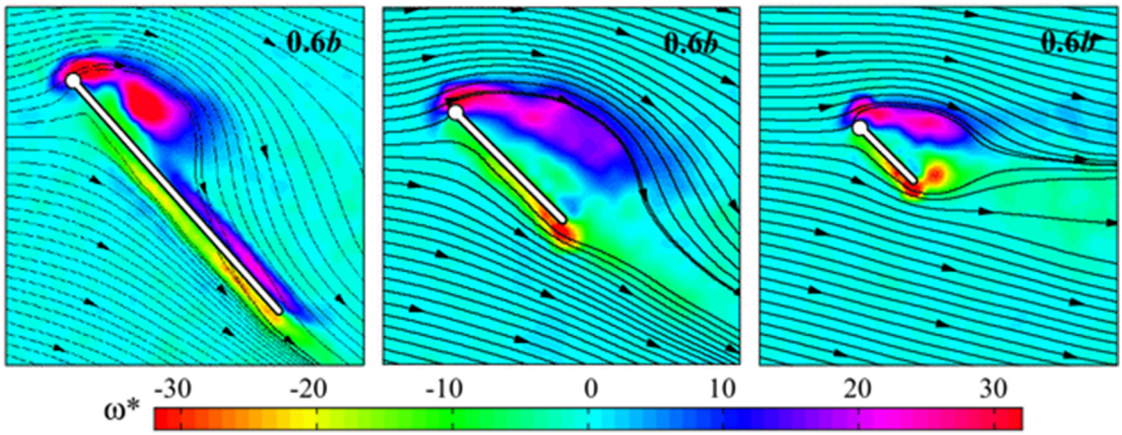

FIG. 6. The contours of the normalized vorticity ($\omega^* = \omega\bar{c}/U_t$) are superimposed with the streamlines of flow over wings of $\mathcal{AR}$ = 1.5, 3, and 6 at r/b = 0.6. Figure adapted with permission from J.-S. Han, J. W. Chang, and H.-K. Cho, "Vortices behavior depending on the aspect ratio of an insect-like flapping wing in hover," Exp. Fluids **56**, 181 (2015). Copyright 2015 Springer Nature.

flow does not reattach. The detachment of the LEV at higher $\mathcal{AR}$ may be due to reduced Coriolis effects, according to Eq. (6). It should be noted that, in this figure, the difference in the LEV structure is shown on the plane at r/b = 0.6. Also, note that the local Rossby numbers for wings of $\mathcal{AR}$ = 1.5, 3, and 6 are r/c = 0.9, 1.8, and 3.6, respectively.

These observations show that important features of the LEV structure change with $\mathcal{AR}$ even when $r/c < 4$. The changes can be seen more clearly in three-dimensional (3D) vortical structures identified by isosurfaces of total pressure,[25] shown in Fig. 7. Here, the LEV over an $\mathcal{AR}$ = 1 wing is a single coherent vortex. With an increase in $\mathcal{AR}$, the LEV core becomes relatively compact, with increased suction beneath it. However, at a certain spanwise location, the LEV expands to a bubblelike structure, which *bursts* to form smaller noncoherent structures. The LEV burst is typically characterized by the spanwise flow stagnation or reversal, the entrainment of the opposite-signed vorticity, and the local expansion of the vortex size.[57] The spanwise locations of the bubble and the LEV burst, both normalized by wingspan, are observed to move inboard with an increase in $\mathcal{AR}$. This weakens the wing-surface suction further outboard, as is clear from the lower magnitude of suction seen outboard. In the case of $\mathcal{AR}$ = 4, the LEV is observed to form narrow dual LEVs that display a helical structure prior to bursting. The narrower size is a result of an increased spanwise flux of vorticity.

Overall, most studies indicate that the spanwise vorticity flux at inboard locations increases with $\mathcal{AR}$. Moreover, the LEV split and bursting occur at a more inboard location for high-$\mathcal{AR}$ wings due to the decreased Coriolis and centripetal effects, consistent with Eq. (6). Although the suction magnitude beneath the LEV increases with $\mathcal{AR}$, the early bursting of the LEV results in a loss of suction outboard. Therefore, according to these observations, the lift coefficient of wings can be expected to increase with $\mathcal{AR}$ up to a limit, beyond which the loss of the outboard suction will dominate, causing the lift coefficient to decrease. Hence, it is of interest to further characterize the effects of $\mathcal{AR}$ on the lift coefficient.

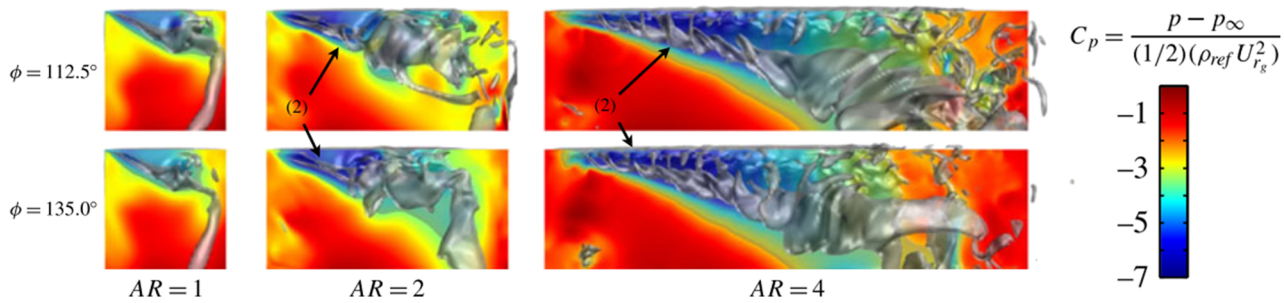

FIG. 7. The 3D LEV structure, identified using the isosurface of total pressure, changes significantly with $\mathcal{AR}$. Contours of the pressure coefficient are shown on the wing suction surface. Figure adapted with permission from D. J. Garmann and M. R. Visbal, "Dynamics of revolving wings for various aspect ratios," J. Fluid Mech. **748**, 932–956 (2014). Copyright 2014 Cambridge University Press.

Published under license by AIP Publishing

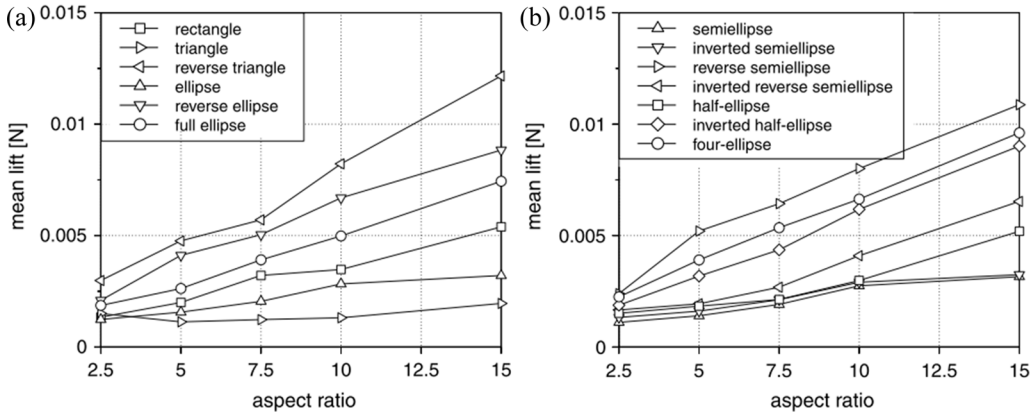

FIG. 8. Relation between lift and $\mathcal{AR}$ for (a) symmetric and (b) asymmetric wing shapes is shown. Figure reproduced with permission from S. A. Ansari, K. Knowles, and R. Zbikowski, "Insectlike flapping wings in the hover. Part I: Effect of wing kinematics," J. Aircr. **45**, 1945–1954 (2008). Copyright 2008 by S. A. Ansari.

B. Effects on the lift coefficient

As discussed earlier, the changes in the flow structure over a wing with $\mathcal{AR}$ are expected to affect the lift (L) acting on the wing. For an assumed value of the lift coefficient (C_L), the expression for L for a given $\mathcal{AR}$ (for a square wing) is given by Ansari *et al.*[58] as

$$L_{\mathcal{AR}} = \frac{1}{2}\rho C_L \omega^2 \bar{c} \frac{b^3}{3}, \tag{7}$$

where ρ is the fluid density and ω is the angular velocity of the wing. It should be noted that the area scaling used in this expression is $b\bar{c}$, which is the same as the wing area S used in most studies. On the other hand, Dickinson and co-workers have used $R\bar{c}$ as the area scaling, where the root cutout is not taken into consideration. If $\mathcal{AR}$ is scaled by a factor of x ($x\mathcal{AR} = xb/\bar{c}$), to maintain the same wing area ($S = b\bar{c}$), the chord and wingspan should be changed to $\bar{c}/\sqrt{x}$ and $b\sqrt{x}$, respectively. Therefore, the lift acting of the scaled wing shape will be

$$L_{x\mathcal{AR}} = \frac{1}{2}\rho C_L \omega^2 \frac{\bar{c}}{\sqrt{x}} \frac{(\sqrt{x}b)^3}{3} = xL_{\mathcal{AR}}. \tag{8}$$

The numerical simulations of Ansari *et al.* have shown that various symmetric and asymmetric wing shapes adhere to the linear relation between L and $\mathcal{AR}$, as can be seen in Fig. 8. This relation is derived under the assumption that C_L remains constant across various $\mathcal{AR}$. However, it may be noted that some shapes, such as the ellipse and semiellipse, do not follow the linear relationship between L and $\mathcal{AR}$. Ansari *et al.* have attributed this deviation to the "hindering effects of the wake-induced components" of the lift for the wings of higher $\mathcal{AR}$.

Moreover, the reference velocity used here is $\sqrt{\omega^2 b^2/3}$. Following the observation that $\hat{r}_2$ of most insect wings is close to $1/\sqrt{3}$ (see Fig. 2), the reference velocity can be expressed as ωr_2. Indeed, using this reference velocity, Luo and Sun showed that the variation in $\mathcal{AR}$ has only a minimal effect on C_L. Their numerical simulations with rotating wings of various $\mathcal{AR}$ showed a negligible effect on C_L at two different Re, as can be seen in Fig. 9, supporting the assumptions of Ansari *et al.* Furthermore, Carr *et al.*[27] also observed C_L to be only slightly decreasing with $\mathcal{AR}$ for rectangular wings rotating with a constant wing tip velocity.

On the other hand, some researchers have observed the lift coefficient C_L and the drag coefficient C_D to be significantly affected

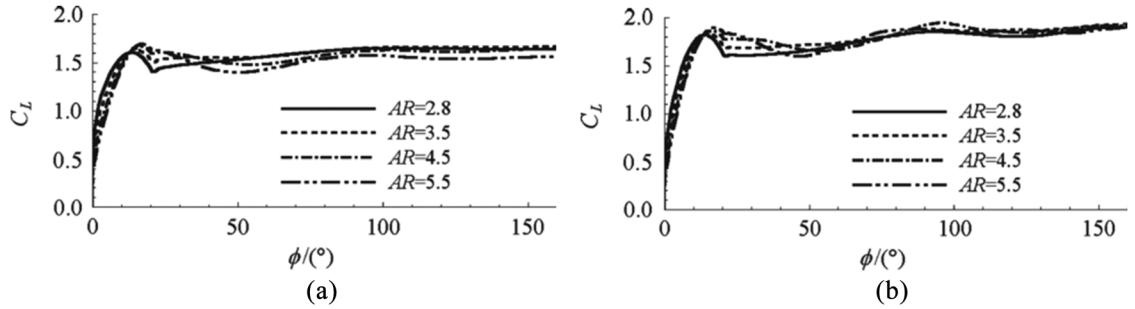

FIG. 9. Variation of C_L with the sweep angle ϕ shows a negligible effect of $\mathcal{AR}$ at (a) Re = 200 and (b) Re = 3500. Figure adapted with permission from G. Luo and M. Sun, "The effects of corrugation and wing planform on the aerodynamic force production of sweeping model insect wings," Acta Mech. Sin. **21**, 531–541 (2005). Copyright 2005 Springer Nature.

Published under license by AIP Publishing

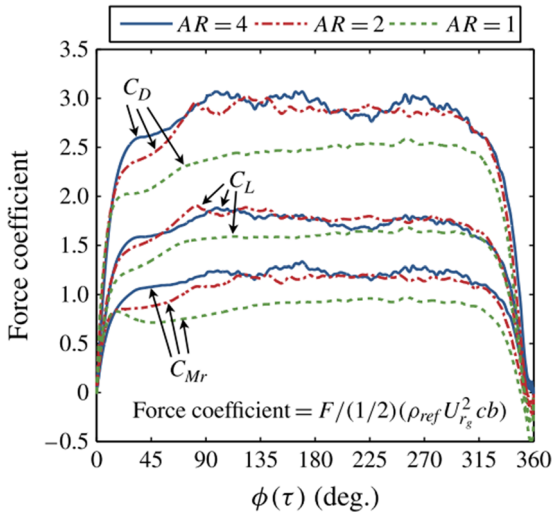

FIG. 10. Variations in force coefficients with the sweep angle are shown for various $\mathcal{AR}$. Figure adapted with permission from D. J. Garmann and M. R. Visbal, "Dynamics of revolving wings for various aspect ratios," J. Fluid Mech. **748**, 932–956 (2014). Copyright 2014 Cambridge University Press.

by $\mathcal{AR}$. Garmann and Visbal,[25] for example, showed that C_L and C_D during the sweep motion are lower for $\mathcal{AR} = 1$ and higher for larger $\mathcal{AR}$. However, there is no significant change in the C_L and C_D values between $\mathcal{AR} = 2$ and $\mathcal{AR} = 4$, as can be seen in Fig. 10.

Han *et al.*[26] extended the range of $\mathcal{AR}$ and observed that increasing $\mathcal{AR}$ beyond the value of 3 results in a reduction in C_L. This variation is similar to the spanwise variation in the LEV circulatory lift reported by Kruyt *et al.*[29] (see Fig. 4). According to these studies, $\mathcal{AR} = 3$ is optimum. Many insects flying at low *Re* have wings of $\mathcal{AR} \approx 3$. However, it should be noted that the experiments in both of these studies were carried out at relatively high Reynolds numbers (~10^4), where a wider range of $\mathcal{AR}$ is observed in insects (see Fig. 2). Hence, the optimization of $\mathcal{AR}$ based on C_L may be insufficient to explain the existence of other aspect ratios in nature.

Although it has been established by researchers, e.g., Luo and Sun,[23] that the velocity at the radius of gyration, U_g, is the appropriate reference velocity, many other researchers, for example, Carr *et al.*[27] and Phillips *et al.*,[28] have used the wing-tip velocity, U_t, as the reference. This choice of reference also affects the trends observed in the lift coefficient as a function of $\mathcal{AR}$. Figure 11 summarizes the trends in the mean lift coefficient based on U_g [i.e., $\overline{C}_L = 2\overline{L}/(\rho U_g^2 S)$, where $\overline{L}$ is the mean lift] and that based on U_t [i.e., $\overline{C}_{L_t} = 2\overline{L}/(\rho U_t^2 S)$] with changing $\mathcal{AR}$ extracted from various studies. It is clear from this figure that not only the actual values of the lift coefficient but also their trends are inconsistent between various studies.

Broadly, the values of $\overline{C}_L$ in these studies are in the range between 1 and 1.8, as can be seen in Fig. 11(a). The data from Han *et al.*[26] and Shahzad *et al.*[30] are outside this range, perhaps due to a difference in scaling, not clear from the available information. Overall, the observed variations in the trends would result in differences in the selection of the optimum aspect ratios based on the maximum $\overline{C}_L$. For example, for Han *et al.*[26] and Jardin and Colonius,[31] $\mathcal{AR} = 3$ is optimum, whereas for Harbig *et al.*,[24] $\mathcal{AR} = 5$ is optimum. Harbig *et al.*[20] and Bhat *et al.*[32] showed a monotonic decrease in $\overline{C}_L$ after a certain value of $\mathcal{AR}$, indicating that a low $\mathcal{AR}$ is optimum. On the other hand, Phillips *et al.*[28] and Shahzad *et al.*[30] showed a monotonic increase in $\overline{C}_L$ with $\mathcal{AR}$.

These variations may be due to the differences in the values of parameters, such as *Re*, the reference scales, the wing shapes, and the angles of attack, which are summarized in Appendix A. It should be noted that Harbig *et al.*,[20] Carr *et al.*,[27] and Bhat *et al.*[32] have used the constant span-based Reynolds number

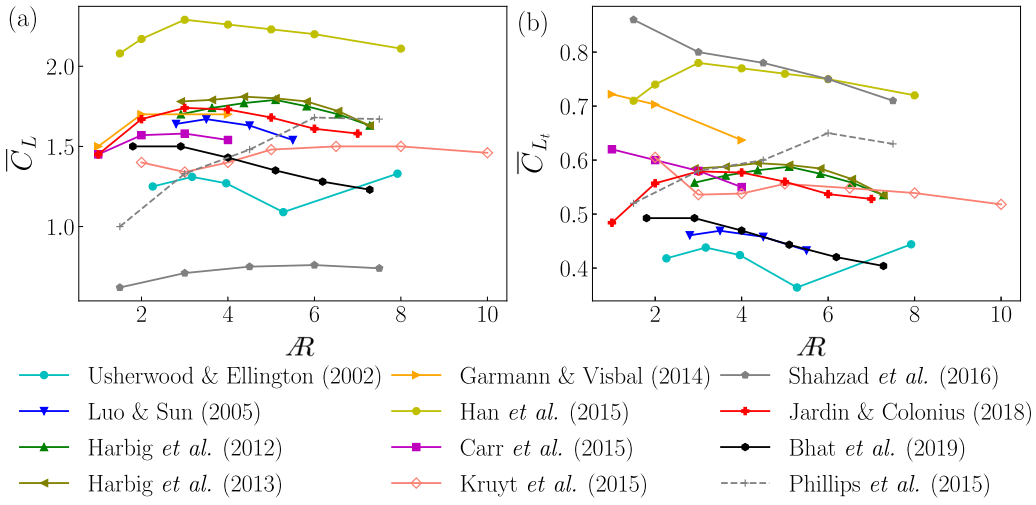

FIG. 11. Comparison of variations in (a) the lift coefficient based on U_g ($\overline{C}_L$) with $\mathcal{AR}$ and of those in (b) the lift coefficient based on U_t ($\overline{C}_{L_t}$) with $\mathcal{AR}$, extracted from various past studies, is shown. The dashed line represents the LEV-circulatory lift coefficient.

Published under license by AIP Publishing

($Re_b = Re \times \mathcal{R}$), which will be discussed later. Moreover, our recent study[32] indicates that $\overline{C}_L$ derived from the LEV-circulatory lift, such as that by Phillips *et al.*,[28] may not represent the actual $\overline{C}_L$ and its trends accurately. Furthermore, the values of $\overline{C}_L$ by Kruyt *et al.*[29] are obtained at relatively high Reynolds numbers ($Re \sim 10^4$) inspired by hummingbird wings. At such *Re*, the variations in $\overline{C}_L$ may not be comparable to those for insect-scale *Re* since bird wings at higher *Re* maintain a lower α and typically have higher $\mathcal{R}$, which makes it easier for them to glide, unlike for insects.

When scaled with U_t, the trends in $\overline{C}_{L_t}$ from most studies show a decrease with $\mathcal{R}$, as can be seen in Fig. 11(b). The difference in the trends in $\overline{C}_{L_t}$ from some studies with respect to the trends in $\overline{C}_L$ is on account of the change in the values of R_g/b with $\mathcal{R}$ in those studies. The relation between $\overline{C}_{L_t}$ and $\overline{C}_L$ can be given by $\overline{C}_{L_t} = \overline{C}_L \times R_g^2/b^2$. For a given wing planform without a root offset, the ratio R_g/b should remain constant even after changing $\mathcal{R}$. However, this ratio may also be affected by the wing offset ratio $\hat{b}_0$, as shown later in Eq. (10). In some studies, the values of R_g/b have changed with $\mathcal{R}$. This has resulted in trends in $\overline{C}_{L_t}$ different to those in $\overline{C}_L$.

C. Coupled effects of $\mathcal{R}$ and other parameters

Aerodynamics of a rotating or a flapping wing is determined by parameters from a large parameter space. There might be many factors, including *Re*, *Ro*, α, and wing shape, that can affect the wing aerodynamics.[13,18,31,59] Kruyt and co-workers, for example, showed that low-$\mathcal{R}$ wings outperform high-$\mathcal{R}$ wings in terms of the aerodynamic forces and power economy if the angle of attack is in the range $\alpha > 20°$. However, at lower angles, the high-$\mathcal{R}$ wings outperform the low-$\mathcal{R}$ wings. Therefore, the values of $\overline{C}_L$ predicted by various researchers may not compare well unless all the affecting variables are maintained to be the same.

For the comparison in Fig. 11, we have tried to extract most results from the studies on wings in pure rotation with $\alpha \sim 45°$. For the flapping wing experiments of Han *et al.*, the values shown were extracted during the wing sweep motion, during which the wing was rotated with a near-constant angular velocity and a constant α. Nevertheless, the values of *Re* from various studies vary over a very large range of $[10^2–10^4]$. Moreover, most computational studies rotate the wings about their roots, whereas most experimental studies require a central body to hold and rotate the wing. The presence of a central body causes the wing to be offset from the rotation axis, changing its Rossby number. Various wing shapes can be described by the characteristic length R_g, which also affects *Ro*. The variations in *Ro* may in turn affect the LEV as well as the forces, depending on the size of the central body.[32,60]

The coupled effects of $\mathcal{R}$ and *Re* were studied systematically by Harbig *et al.*[20] They observed that the large-scale vortical structures over a rotating wing change with both $\mathcal{R}$ and *Re*. As can be seen in Figs. 12(a)–12(c), a single LEV is observed at a low *Re*, which is observed to split into the dual LEVs, namely, LEV1 and LEV2, at higher *Re*. The reason of the split has been attributed to the growth of the secondary vortex (SV) beneath the LEV between the two corotating vortex cores. As *Re* increases, the strength of the SV also increases, causing the LEV to split at a more inboard location. This split is followed by vortex bursting at a certain spanwise location. It should be noted that the LEV structures in these figures have been shown as the isosurfaces of the constant *Q* value.[20]

Interestingly, Harbig and co-workers observed a similar phenomenon even with an increase in $\mathcal{R}$ and a constant *Re*,

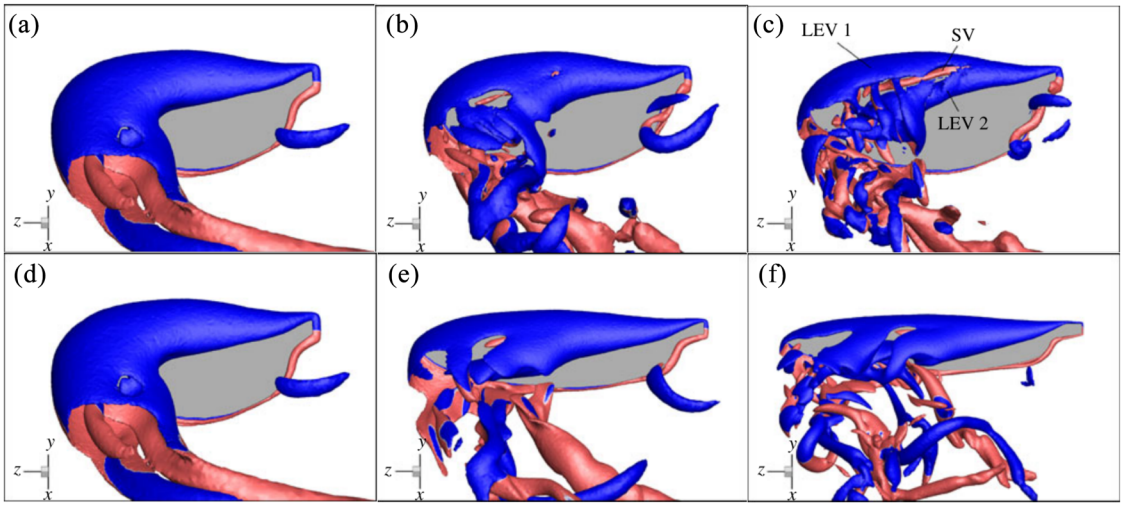

FIG. 12. The LEV structures identified by the isosurfaces of Q over a rotating wing of $\mathcal{R} = 2.91$ are shown at (a) *Re* = 300, (b) *Re* = 750, and (c) *Re* = 1500. Furthermore, the LEV structures over wings of (d) $\mathcal{R} = 2.91$, (e) $\mathcal{R} = 5.1$, and (f) $\mathcal{R} = 7.28$ are shown for *Re* = 300. Figure adapted with permission from R. R. Harbig, J. Sheridan, and M. C. Thompson, "Reynolds number and aspect ratio effects on the leading-edge vortex for rotating insect wing planforms," J. Fluid Mech. **717**, 166–192 (2013). Copyright 2013 Cambridge University Press.

Published under license by AIP Publishing

similar to that observed by Luo and Sun[23] and Garmann and Visbal.[25] As can be seen in Figs. 12(d)–12(f), at Re = 300, the LEV splits at higher $\mathcal{AR}$ and the split location shifts inboard with an increase in $\mathcal{AR}$. Harbig and co-workers tracked the LEV split location by systematically varying both Re and $\mathcal{AR}$ over a wide range. From their study, they successfully attempted to decouple the effects of the two parameters by suggesting the wingspan as an alternate length scale for the Reynolds number. According to their suggestion, the span-based Reynolds number is defined as

$$Re_b = U_g b/\nu. \tag{9}$$

Note that the length scale $\bar{c}$ from Eq. (4) has been replaced with b. With this modified definition, Harbig and co-workers showed that the LEV split occurs at approximately the same spanwise location across a range of $\mathcal{AR}$ at constant Re_b. This, in turn, shows that the large-scale vortical structure remains independent of $\mathcal{AR}$ if Re_b is maintained to be constant. Carr *et al.*[27] also followed the span-based definition of Re and showed that the spanwise circulation around the LEV at a high rotation angle (ϕ = 120°) was minimally affected between $\mathcal{AR}$ = 2 and $\mathcal{AR}$ = 4.

Furthermore, Lee *et al.*[21] found the effects of Ro and $\mathcal{AR}$ also to be coupled. This is because, for the wings with a root offset, the relation between Ro and $\mathcal{AR}$ is affected by the wing-root offset distance. For the wing models with the normalized root offset of $\hat{b}_0 = b_0/b$ from the rotation axis, the radius of gyration can be approximated to $R_g \approx b\sqrt{\hat{r}_2'^2 + \hat{b}_0 + \hat{b}_0^2}$, where $\hat{r}_2'$ is the normalized radius of the second moment of area of the wing without any offset. Therefore, the Rossby number in this case will be

$$Ro \approx \mathcal{AR}\sqrt{\hat{r}_2'^2 + \hat{b}_0 + \hat{b}_0^2}. \tag{10}$$

This shows that, for a given wing planform (i.e., a constant $\hat{r}_2'$) and a constant wing offset ratio (i.e., a constant $\hat{b}_0$), Ro changes linearly with $\mathcal{AR}$. However, in some experimental studies, $\hat{b}_0$ also changes with a change in $\mathcal{AR}$ due to the extension of the wingspan. Hence, the variations in Ro in these studies were different from those with a constant $\hat{b}_0$. This could have resulted in differences in the perceived effects of $\mathcal{AR}$ in various studies.

D. Reconciling the past studies

The first attempt to reconcile the past studies was undertaken in a remarkable study by Lee *et al.*[21] They classified previous studies into two groups, depending on their offsets. The first group involved the "*constant* $\hat{r}_2$ *configurations*" of Usherwood and Ellington,[22] Luo and Sun,[23] and Han *et al.*[26] The second group involved the "*constant* ΔR *configurations*" or, consistent with the present notation, the "*constant* b_0 *configurations*" of Garmann and Visbal,[25] Carr *et al.*,[27] Phillips *et al.*,[28] and Kruyt *et al.*[29] The variations in Ro with respect to $\mathcal{AR}$ in all of these studies were different.

In order to reveal the coupling between Ro and $\mathcal{AR}$, Lee and co-workers simulated four series of configurations. Series-1 was the *root-flapping series* with $\hat{b}_0$ = 0, in which $\mathcal{AR}$ was varied by extending the wingspan. Series-2 involved a constant b_0, while $\mathcal{AR}$ was varied by extending the wing chord. Series-3 also involved a constant b_0; however, $\mathcal{AR}$ was varied by changing the wingspan, thereby simultaneously changing $\hat{b}_0$. Series-4 was the *constant Ro series*, in which b_0 was changed for each $\mathcal{AR}$ such that Ro remained constant across different $\mathcal{AR}$. By varying both $\mathcal{AR}$ and Ro over large ranges, Lee and co-workers obtained a map of the predictions of $\overline{C}_L$ on the plane of $\mathcal{AR}$ and Ro, as shown in Fig. 13(a). These contours are superimposed with the lines showing the variations in $\mathcal{AR}$ and Ro in Series-1 to 4. Depending on these variations, the relation between $\overline{C}_L$ and $\mathcal{AR}$ may vary, as can be seen

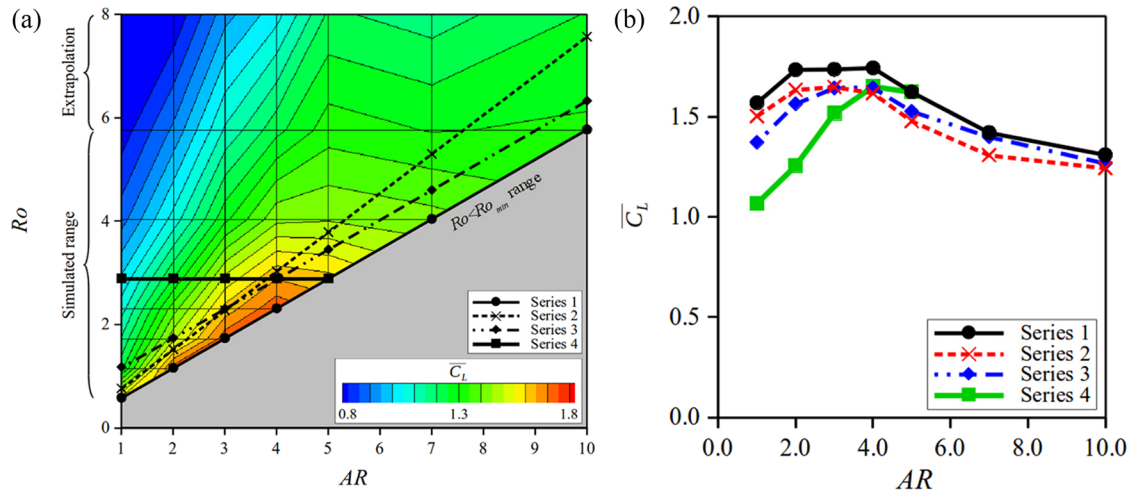

FIG. 13. In (a), contours of $\overline{C}_L$ are mapped on the plane of $\mathcal{AR}$ and Ro. In (b), the variations in $\overline{C}_L$ with $\mathcal{AR}$ are shown for various series of configurations. Figures adapted with permission from Y. J. Lee, K. B. Lua, and T. T. Lim, "Aspect ratio effects on revolving wings with Rossby number consideration," Bioinspiration Biomimetics **11**, 056013 (2016). Copyright 2016 IOP Publishing.

Published under license by AIP Publishing

in Fig. 13(b). Therefore, the choice of optimum $\mathcal{AR}$ may change with the series.

It should be noted that all the configurations in this study were simulated at Re = 500, which is close to Re of only small insects. At this Re, the phenomenon of the LEV-splitting and LEV-bursting can be observed only for relatively very high $\mathcal{AR}$. However, for larger insects with higher Re, the LEV split can be observed even at low $\mathcal{AR}$ (see Lu *et al.*[56]), which can affect the variation in $\overline{C}_L$. Moreover, most experimental studies are conducted at higher Re due to limitations in the force measurements at low Re. Looking at the large variation in Re across various past studies, an investigation of the combined effects of $\mathcal{AR}$, Ro, and Re was thought necessary to reconcile those studies.

In our recent work,[32] the individual as well as combined effects of these three important parameters were studied. First, the effect of the span-based Reynolds number on $\overline{C}_L$ was investigated. The increase in $\overline{C}_L$ with Re_b was very high in the lower range of Re_b, as can be seen in Fig. 14(a). At higher Re_b, $\overline{C}_L$ changed by only small amount. The increase in $\overline{C}_L$ was due to the increased LEV suction as a result of the higher vorticity magnitudes with increasing Re_b. However, at high Re_b, the induced LEV bursting and splitting resulted in a loss of sectional suction, causing only a small increase in overall suction. As expected, the variation in $\overline{C}_L$ was found to be also sensitive to Ro maintaining a similar trend with Re_b.

The individual effect of Ro was observed by investigating a large range of Ro at fixed values of Re_b. For the wing of $\mathcal{AR}$ = 2.91, extending Ro over a larger range showed a monotonic decrease in $\overline{C}_L$, as shown in Fig. 14(b). This decrease was due to the weaker LEV as a result of the reduced Coriolis acceleration[17,18] at high Ro. Here, $\mathcal{AR}$ of the wing was maintained to be constant. However, Bhat *et al.*[32] found the LEV structures to vary with $\mathcal{AR}$, even at a constant Ro. This is because, to maintain the same Ro, the offset $\hat{b}_0$ had to be adjusted with a change in $\mathcal{AR}$ [see Eq. (10)]. Various wing root offsets caused the Coriolis accelerations to vary across $\mathcal{AR}$ even with a constant Ro. As Ro was insufficient in correlating the Coriolis acceleration with $\mathcal{AR}$, the scaling of Ro was revisited.

Since it was established that the wingspan was better correlated with the LEV structure, the Navier-Stokes equations for a wing in a rotating frame of reference were rescaled using b as the reference length scale. In this case, the vector equation reduces to

$$\frac{D\boldsymbol{u}}{Dt} + \frac{(\dot{\Omega}/\Omega^2)}{(R_g/b)^2}\dot{\boldsymbol{\Omega}}\times\boldsymbol{r} + \frac{1}{(R_g/b)^2}\boldsymbol{\Omega}\times(\boldsymbol{\Omega}\times\boldsymbol{r}) + \frac{2}{(R_g/b)}\boldsymbol{\Omega}\times\boldsymbol{u} = -\nabla p + \frac{\mu}{\rho U_g b}\nabla^2\boldsymbol{u}. \tag{11}$$

As expected, the viscous term scales with $Re_b = \rho U_g b/\mu$. Importantly, the Coriolis acceleration scaled with R_g/b, suggesting a span-based definition for the Rossby number, i.e., $Ro_b = R_g/b$. Using this, it was confirmed that the LEV structure across various $\mathcal{AR}$ remains similar at a constant Ro_b.[32]

Using the modified scaling, the work of Harbig and co-workers was extended to study wider ranges of both $\mathcal{AR}$ and Re. It can be seen in Fig. 14(c) that, at a constant Re_b, $\overline{C}_L$ increases by a small amount in the low range of $\mathcal{AR}$ and then suddenly decreases beyond a certain value in a higher range. In other words, at any given Re_b, $\overline{C}_L$ is less sensitive to $\mathcal{AR}$ only over a certain range. Interestingly, this range widens with an increase in Re_b. If this range of $\mathcal{AR}$ is considered to be optimum purely based on $\overline{C}_L$, the optimum range covers only smaller $\mathcal{AR}$ at small Re_b and a wider range of $\mathcal{AR}$ at higher Re_b. Coincidentally, these optimum ranges overlap the values of $\mathcal{AR}$ found in nature at the respective Re_b, which might be one of the important reasons behind the presence of a wide variety of $\mathcal{AR}$ at higher Re_b.

With an increase in $\mathcal{AR}$, with b as the reference, the mean wing chord decreases. This causes a reduction in the area available for supporting the LEV. Beyond a certain critical value of $\mathcal{AR}$, the LEV hits the trailing edge and interacts with opposite sign vorticity from the trailing edge (TEV). This interaction weakens the LEV and reduces the suction over the wing. Therefore, at $\mathcal{AR}$ larger than the critical value, $\overline{C}_L$ suddenly drops. It should be noted that, at higher Re_b, the LEV is narrower due to the increased spanwise vorticity transport. Therefore, the LEV remains less affected

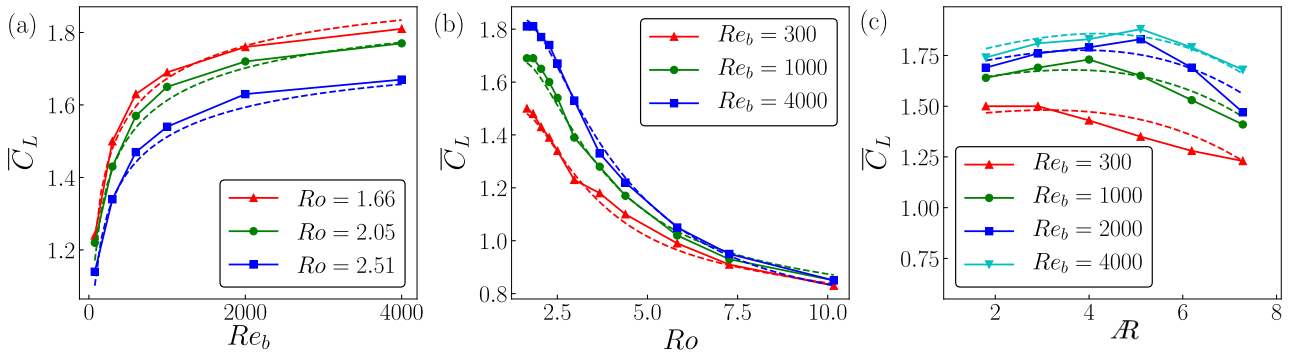

FIG. 14. The coupled effects of Re_b, Ro_b, and $\mathcal{AR}$ on $\overline{C}_L$. Data extracted with permission from Bhat *et al.*, "Uncoupling the effects of aspect ratio, Reynolds number and Rossby number on a rotating insect-wing planform," J. Fluid Mech. **859**, 921–948 (2019). Copyright 2019 Cambridge University Press. The dashed lines indicate predictions using the polynomial fit to the data. The wing aspect ratio in (a) and (b) is $\mathcal{AR}$ = 2.91. The Rossby number in (c) is Ro = 1.66.

Published under license by AIP Publishing

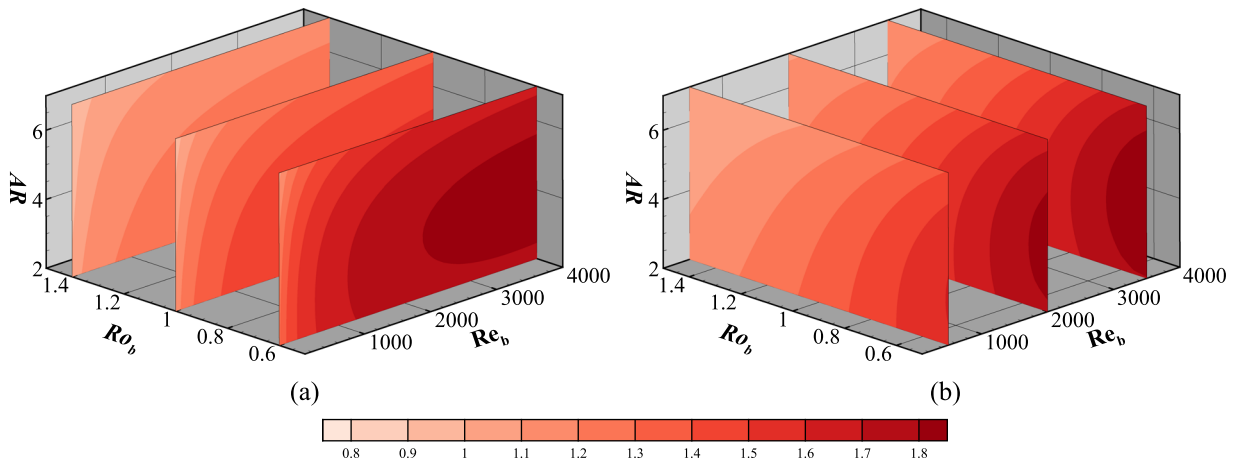

FIG. 15. The contours of $\overline{C}_L$, predicted using the polynomial model, are shown in the 3D space of $\mathcal{AR}$, Re_b, and Ro_b in (a) on the $\mathcal{AR} - Re_b$ planes at Ro_b = 0.6, 1, and 1.4 and in (b) on the $\mathcal{AR} - Ro_b$ planes at Re_b = 500, 2000, and 3500.

by the TEV over a wider range of $\mathcal{AR}$, which results in a wider optimal range.

Overall, this shows that $\overline{C}_L$ has a coupled effect of Re_b, Ro_b, and $\mathcal{AR}$. Based on our CFD data obtained from exploring a wide three-dimensional parameter space (of ~100 points), a polynomial model $\overline{C}_L = f_1(Re_b, Ro_b, \mathcal{AR})$ was derived using cross-validation and LASSO regularization. The predictions of $\overline{C}_L$ using this model are plotted as dashed lines in Fig. 14. Using the same model, the values of $\overline{C}_L$ were predicted in the 3D parameter space of $\mathcal{AR}$, Re_b, and Ro_b. The contours of $\overline{C}_L$ on various planes in this space can be seen in Fig. 15. Clearly, the maximum possible $\overline{C}_L$ can be observed at a low Ro_b and a high Re_b.

Finally, an attempt was made to reconcile the seemingly inconsistent trends in $\overline{C}_L$ with $\mathcal{AR}$ from previous studies [see Fig. 11(a)] by observing the relative variations in Re_b and Ro_b. Using their values of $\mathcal{AR}$, Re_b, and Ro_b, the values of $\overline{C}_L$ were predicted with the polynomial model and compared with their data, as can be seen in Fig. 16. The model could predict the values of $\overline{C}_L$ within 10% accuracy, approximately, for most of the past results. Although the predictions deviate from the data of Usherwood and Ellington[22] and Carr *et al.*[27] at a few points, overall, the model appears to predict the values well. Some deviations in the predictions are observed for the higher range of $\mathcal{AR}$ in the cases of Luo and Sun,[23] Garmann and Visbal,[25] and Jardin and Colonius.[31] This might be owing to the fact that α used by Luo and Sun[23] and Garmann and Visbal[25] are 40° and 60°, respectively, whereas the present model is based on the cases with α = 45°. Moreover, the lift in the high-$\mathcal{AR}$ cases of Jardin and Colonius[31] had not

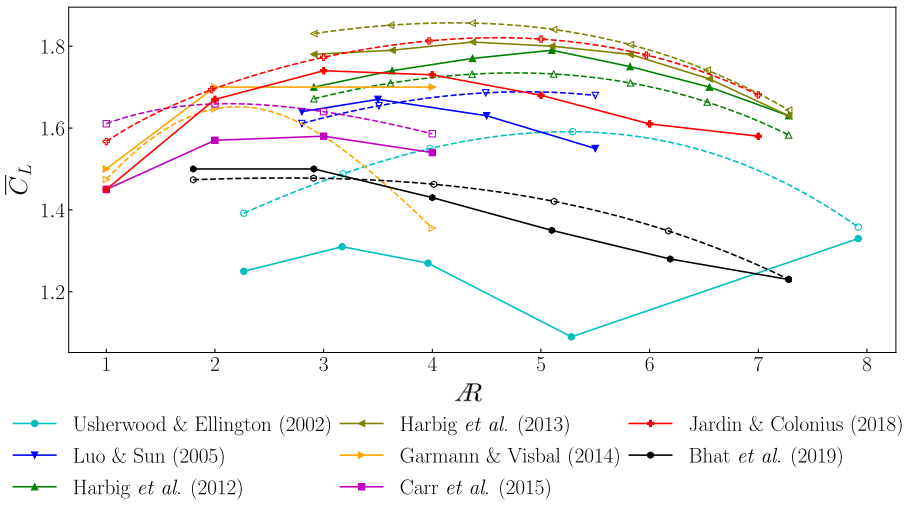

FIG. 16. The variations in $\overline{C}_L$ reported by previous researchers are compared with the predictions using the polynomial model, shown by open symbols and dashed lines of the corresponding colors.

Published under license by AIP Publishing

stabilized even after the rotation of 180°, unlike that observed in other studies.

Broadly, it can be concluded that consideration of the combined effects of $\mathcal{AR}$, Re_b, and Ro_b helps reconcile seemingly conflicting past aspect-ratio studies. It is also clear from this study that direct comparisons of the results from previous studies can be made only when the values of their $\mathcal{AR}$, Re_b, and Ro_b are matched.

It should be noted that the data of Shahzad *et al.* and Phillips *et al.* have not been included in the comparison due to ambiguity in their $\overline{C}_L$ values as mentioned earlier. Moreover, the present model does not predict the $\overline{C}_L$ values well for Re_b in a higher range ($>10^5$), such as those in the case of Han *et al.* (2015) and Kruyt *et al.*[29] Further exploration of this range of Re_b is necessary, first, to verify whether the span-based scaling governs the flow physics well even in this range and/or, second, to derive or modify the model to predict $\overline{C}_L$ accurately in this range of Re_b.

E. Future directions

It should be noted that the present analysis is indeed limited to the hovering wings. In the case of the forward flight, the advance ratio, i.e., the ratio of the forward speed to the mean wing tip velocity ($J = V/U_t$), is considered to be an additional parameter that affects the mean lift.[6,61] Given a mean reference velocity, an increase in J causes the mean lift coefficient to decrease.[62] J and $\mathcal{AR}$ have been found to have coupled effects on the mean lift coefficient and the LEV stability. Hence, the present model will have to be modified to include the effects of J. Moreover, the wing flexibility has been observed to enhance $\overline{C}_L$,[63] which should be taken into consideration while predicting $\overline{C}_L$ for flexible wings.

The present model predicts broadly consistent $\overline{C}_L$ in the investigated ranges of $\mathcal{AR}$, Re_b, and Ro_b. However, at very high Re_b, the LEV over high-$\mathcal{AR}$ wings will tend to be more unstable, resulting in an early burst. Beyond a certain range, the effect of wingspan will be insignificant and the flow will approach that over a two-dimensional wing, where the span-based scaling of LEV may not be applicable. An extended range of Re_b needs to be explored in future to investigate the transition from the span-based scaling to the chord-based scaling. Moreover, at very low Re_b, the L/D ratio drops rapidly and the viscous diffusion effects are very large, affecting the LEV structure.[64] It might be interesting to see whether the span-based scaling can be applied to the flow at such low Re_b.

Furthermore, the present model is developed based on the constant angle of attack ($\alpha = 45°$). Some previous studies[23,25] have incorporated different α, for which the present model may not predict the forces accurately. Moreover, Kruyt *et al.*[29] have shown that, at high Re, large-$\mathcal{AR}$ wings benefit from lower angles of attack to achieve high L/D ratios. Hence, the present model might be improved by combining the results, for example, of Sane and Dickinson[65] to involve the effect of α on the aerodynamic forces.

Finally, the understanding of the physics behind the LEV development, its growth, and burst is important in understanding its effects on the aerodynamic forces. The analysis of various terms in the vorticity transport equation applied to the LEV for various $\mathcal{AR}$, Re_b, and Ro_b might help linearize the functions $f(\mathcal{AR})$, $g(Re_b)$, and $h(Ro_b)$ (see Appendix C), which in turn will result in fewer polynomial terms of the model. Hence, the present empirical polynomial model might be simplified using this detailed analysis.

IV. CONCLUDING REMARKS

This review presents a comprehensive overview of previous studies on insect-wing aspect ratios. Measurements of real insect wings show that there is a wide variety of aspect ratios found in nature. In terms of flow structures, studies presenting the effects of $\mathcal{AR}$ over rotating or flapping wings are broadly consistent. The leading-edge vortex (LEV) over a wing, which is responsible for the high lift, is observed to split at higher $\mathcal{AR}$. Moreover, the increase in the LEV cross-sectional size along the span causes the LEV to reach the trailing edge without reattaching and then weaken through the influence of the opposite sign vorticity from the trailing edge for $\mathcal{AR} > 3$. Thus, some studies predict $\mathcal{AR} = 3$ to be optimal based on the mean lift coefficient of the wing ($\overline{C}_L$). On the other hand, other studies present different conclusions. The inconsistencies in these trends have been reviewed by further studies, which indeed reveal that they are due to the coupled effects of the simultaneous but different variations in Reynolds and Rossby numbers between sets of experiments. Taking this further, recent work shows that the flow structure over an insect wing better correlates with modified Reynolds and Rossby numbers based on wingspan. Moreover, this scaling also helps better reconcile apparent differences in the $\overline{C}_L$-$\mathcal{AR}$ trends recorded in a variety of previous studies. This review highlights that the direct comparisons of the previous results showing $\mathcal{AR}$ effects on the wing aerodynamics are only possible if the values of the aspect ratio, Reynolds number, and Rossby number are matched.

ACKNOWLEDGMENTS

The authors acknowledge a generous computing time allocation from the National Computational Infrastructure (NCI) and Pawsey Supercomputer Centre (NCMAS Merit Grant Nos. n67 and d71) and support through the Australian Research Council (Grant Nos. DP170100275 and DP190103388).

APPENDIX A: DATA FROM PREVIOUS STUDIES

The data for the geometrical and kinematic parameters of wing models in various aspect-ratio studies have been shown in Table I. The symbol $*$ denotes the values calculated based on the available data.

APPENDIX B: INSECT WING GEOMETRIES AND KINEMATICS

The data for the geometrical and kinematic parameters of various insects mentioned in previous studies have been summarized in Table II.

Published under license by AIP Publishing

TABLE I. Data from previous studies. * denotes the values calculated based on the available data.

Literature	Wing shape	EXP/CFD	$\hat{r}_2(S)$	$\mathcal{R}$	$\hat{b}_0$	R_g/b	R_g/c	$R_g/(b+b_0)$	α°	$Re_t = U_t c/\nu$	$Re = U_g c/\nu$	$Re_b = U_g b/\nu$	C_{L_t}	C_L	Remarks
Usherwood and Ellington (2002)	Bumblebee	EXP (rotating)	0.541	2.3	0.103*	0.638*	1.444*	0.578	45	11 295	6529*	14 787*	0.418*	1.25	Extracted C_v (steady) for 45°
			0.541	3.2	0.103*	0.638*	2.022*	0.578	45	8 071	4665*	14 788*	0.438*	1.31	Extracted C_v (steady) for 45°
			0.541	4.0	0.103*	0.638*	2.525*	0.578	45	6 461	3734*	14 788*	0.424*	1.27	Extracted C_v (steady) for 45°
			0.541	5.3	0.103*	0.638*	3.367*	0.578	45	4 846	2801*	14 789*	0.364*	1.09	Extracted C_v (steady) for 45°
			0.541	7.9	0.103*	0.638*	5.051*	0.578	45	3 230	1867*	14 786*	0.444*	1.33	Extracted C_v (steady) for 45°
Luo and Sun (2005)	Hawkmoth	CFD (rotating)	0.530	2.8	0	0.530*	1.484*	0.530*	40		200	560*	0.461*	1.64	Extracted from timetraces
			0.530	3.5	0	0.530*	1.855*	0.530*	40		200	700*	0.469*	1.67	Extracted from timetraces
			0.530	4.5	0	0.530*	2.385*	0.530*	40		200	900*	0.458*	1.63	Extracted from timetraces
			0.530	5.5	0	0.530*	2.915*	0.530*	40		200	1 100*	0.435*	1.55	Extracted from timetraces
Harbig *et al.* (2012)	Fruit fly	CFD (rotating)	0.573	2.9	0	0.573*	1.667*	0.573*	45		300	873*	0.558*	1.70	Direct datapoints
			0.573	3.6	0	0.573*	2.079*	0.573*	45		300	1 089*	0.571*	1.74	Direct datapoints
			0.573	4.4	0	0.573*	2.503*	0.573*	45		300	1 311*	0.581*	1.77	Direct datapoints
			0.573	5.1	0	0.573*	2.921*	0.573*	45		300	1 530*	0.587*	1.79	Direct datapoints
			0.573	5.8	0	0.573*	3.333*	0.573*	45		300	1 746*	0.574*	1.75	Direct datapoints
			0.573	6.6	0	0.573*	3.751*	0.573*	45		300	1 965*	0.558*	1.70	Direct datapoints
			0.573	7.3	0	0.573*	4.169*	0.573*	45		300	2 184*	0.535*	1.63	Direct datapoints
Harbig *et al.* (2013)	Fruit fly	CFD (rotating)	0.573	2.9	0	0.573*	1.667*	0.573*	45		1317*	3833	0.584*	1.78	Direct datapoints
			0.573	3.6	0	0.573*	2.079*	0.573*	45		1056*	3833	0.587*	1.79	Direct datapoints
			0.573	4.4	0	0.573*	2.503*	0.573*	45		877*	3833	0.594*	1.81	Direct datapoints
			0.573	5.1	0	0.573*	2.921*	0.573*	45		752*	3833	0.590*	1.80	Direct datapoints
			0.573	5.8	0	0.573*	3.333*	0.573*	45		659*	3833	0.584*	1.78	Direct datapoints
			0.573	6.6	0	0.573*	3.751*	0.573*	45		585*	3833	0.564*	1.72	Direct datapoints
			0.573	7.3	0	0.573*	4.169*	0.573*	45		527*	3833	0.535*	1.63	Direct datapoints
Garmann and Visbal (2014)	Rectangle	CFD (rotating)	0.577	1.0	0.500*	1.041*	1.041*	0.694*	60		2000	2 000*	0.722*	1.50	Extracted from timetraces
			0.577	2.0	0.250*	0.804*	1.607*	0.643*	60		3000	6 000*	0.703*	1.70	Extracted from timetraces
			0.577	4.0	0.125*	0.688*	2.754*	0.612*	60		5000	20 000*	0.637*	1.70	Extracted from timetraces
Han *et al.* (2015)	Half-ellipse	EXP (flapping)	0.500	1.5	0.200	0.700*	1.050*	0.583*	45	8200	4783*	7 175*	0.600	1.76*	Direct datapoints (translation)
			0.500	2.0	0.200	0.700*	1.400*	0.583*	45	8200	4783*	9 567*	0.590	1.73*	Direct datapoints (translation)
			0.500	3.0	0.200	0.700*	2.100*	0.583*	45	8200	4783*	14 350*	0.590	1.73*	Direct datapoints (translation)
			0.500	4.0	0.200	0.700*	2.800*	0.583*	45	8200	4783*	19 133*	0.580	1.70*	Direct datapoints (translation)
			0.500	5.0	0.200	0.700*	3.500*	0.583*	45	8200	4783*	23 917*	0.570	1.68*	Direct datapoints (translation)
			0.500	6.0	0.200	0.700*	4.200*	0.583*	45	8200	4783*	28 700*	0.560	1.65*	Direct datapoints (translation)
			0.500	8.0	0.200	0.700*	5.600*	0.583*	45	8200	4783*	38 267*	0.540	1.59*	Direct datapoints (translation)
Carr *et al.* (2015)	Rectangle	EXP (rotating)	0.577	1.0	0.300	0.850*	0.850*	0.654*	45	5 780	3781*	3 781*	0.620*	1.45	Extracted from timetraces
			0.577	2.0	0.150	0.711*	1.422*	0.618*	45	5 780	3575*	7 149*	0.600*	1.57	Extracted from timetraces
			0.577	3.0	0.100	0.666*	1.997*	0.605*	45	5 780	3499*	10 496*	0.580*	1.58	Extracted from timetraces
			0.577	4.0	0.075	0.643*	2.574*	0.599*	45	5 780	3459*	13 838*	0.550*	1.54	Extracted from timetraces

Published under license by AIP Publishing

TABLE I. (*Continued.*)

Literature	Wing shape	EXP/CFD	$\hat{r}_2(S)$	$\mathcal{AR}$	$\hat{b}_0$	R_g/b	R_g/c	$R_g/(b+b_0)$	α°	$Re_t = U_t c/\nu$	$Re = U_g c/\nu$	$Re_b = U_g b/\nu$	C_{L_t}	C_L	Remarks
Kruyt *et al.* (2015)	Rectangle	EXP (rotating)	0.577	2.0	0.317	0.866*	1.732*	0.658*	45	11 000	7236*	14 473*	0.605*	1.40	Extracted for $\alpha = 45^\circ$
			0.577	3.0	0.211	0.767*	2.302*	0.634*	45	11 000	6971*	20 912*	0.536*	1.34	Extracted for $\alpha = 45^\circ$
			0.577	4.0	0.158	0.719*	2.875*	0.621*	45	11 000	6826*	27 306*	0.538*	1.40	Extracted for $\alpha = 45^\circ$
			0.577	5.0	0.127	0.690*	3.450*	0.612*	45	11 000	6736*	33 681*	0.556*	1.48	Extracted for $\alpha = 45^\circ$
			0.577	6.5	0.097	0.664*	4.313*	0.605*	45	11 000	6651*	43 230*	0.548*	1.50	Extracted for $\alpha = 45^\circ$
			0.577	8.0	0.079	0.647*	5.177*	0.600*	45	11 000	6596*	52 769*	0.539*	1.50	Extracted for $\alpha = 45^\circ$
			0.577	10.0	0.063	0.633*	6.330*	0.595*	45	11 000	6548*	65 482*	0.518*	1.46	Extracted for $\alpha = 45^\circ$
Shahzad *et al.* (2016)	Beta function	CFD (rotating)	0.584	1.5	0	0.584*	0.876*	0.584*	45	400	233*	350*	0.860	1.53	Direct datapoints
			0.584	3.0	0	0.584*	1.734*	0.584*	45	400	233*	693*	0.800	1.76	Direct datapoints
			0.584	4.5	0	0.584*	2.632*	0.584*	45	400	233*	1 053*	0.780	1.85	Direct datapoints
			0.584	6.0	0	0.584*	3.514*	0.584*	45	400	233*	1 406*	0.750	1.86	Direct datapoints
			0.584	7.5	0	0.584*	4.378*	0.584*	45	400	233*	1 751*	0.710	1.82	Direct datapoints
Jardin and Colonius (2018)	Rectangle	CFD (rotating)	0.577	1.0	0	0.577*	0.577*	0.577*	45		577	577*	0.484*	1.45	Direct datapoints
			0.577	2.0	0	0.577*	1.155*	0.577*	45		577	1 154*	0.557*	1.67	Direct datapoints
			0.577	3.0	0	0.577*	1.732*	0.577*	45		577	1 731*	0.579*	1.74	Direct datapoints
			0.577	4.0	0	0.577*	2.309*	0.577*	45		577	2 308*	0.577*	1.73	Direct datapoints
			0.577	5.0	0	0.577*	2.887*	0.577*	45		577	2 885*	0.560*	1.68	Direct datapoints
			0.577	6.0	0	0.577*	3.464*	0.577*	45		577	3 462*	0.537*	1.61	Direct datapoints
			0.577	7.0	0	0.577*	4.041*	0.577*	45		577	4 039*	0.528*	1.58	Direct datapoints
Bhat *et al.* (2019)	Fruit fly	CFD (rotating)	0.573	1.8	0	0.573	1.031*	0.573*	45		167*	300	0.492*	1.50	Direct datapoints
			0.573	2.9	0	0.573	1.667*	0.573*	45		103*	300	0.492*	1.50	Direct datapoints
			0.573	4.0	0	0.573	2.291*	0.573*	45		75*	300	0.469*	1.43	Direct datapoints
			0.573	5.1	0	0.573	2.921*	0.573*	45		59*	300	0.443*	1.35	Direct datapoints
			0.573	6.2	0	0.573	3.545*	0.573*	45		48*	300	0.420*	1.28	Direct datapoints
			0.573	7.3	0	0.573	4.169*	0.573*	45		41*	300	0.403*	1.23	Direct datapoints
Phillips *et al.* (2015)	Rectangle	EXP (flapping)	0.577	1.5	0.667	1.202*	1.803*	0.721*	45	1400	1010*	1514*	0.520	1.00*	LEV lift
			0.577	3.0	0.333	0.882*	2.646*	0.661*	45	1400	926*	2778*	0.580	1.33*	LEV lift
			0.577	4.5	0.222	0.778*	3.500*	0.636*	45	1400	891*	4009*	0.600	1.48*	LEV lift
			0.577	6.0	0.167	0.726*	4.359*	0.623*	45	1400	872*	5231*	0.650	1.68*	LEV lift
			0.577	7.5	0.133	0.696*	5.220*	0.614*	45	1400	860*	6448*	0.630	1.67*	LEV lift

Published under license by AIP Publishing

TABLE II. Insect data obtained from the work of Weis-Fogh,[4] Ellington,[35] Ennos,[66] and Zanker.[46]

Literature	Animal	n (Hz)	$2\phi_A$ (rad)	b (mm)	$\mathcal{AR}$	Re	$\hat{r}_2$
Weis-Fogh (1973)	Plecotus auritus	13	2.09	120	2.09	14 000	0.500
	Archilochus colubris	52	2.09	45	3.00	6 400	0.500
	Amaxilia fimbriata fluviatilis	35	2.09	59	2.95	7 500	0.500
	Patagonia gigas	15	2.09	130	3.02	15 000	0.500
	Melolontha vulgaris	62	3.14	28	2.80	4 700	0.500
	Amphimallon solstitiale	78	3.14	20	2.86	3 000	0.500
	Heliocopris sp.	38	3.14	70	2.92	17 000	0.500
	Heliocopris sp.	41	3.14	77	2.85	23 000	0.500
	Cetonia aurata	103	3.14	22	3.14	4 300	0.500
	Cerambycidae species	80	3.14	15.5	3.23	1 600	0.500
	Sphinx lingustri	30	2.09	50	2.17	6 300	0.500
	Manduca sexta	27	2.09	54	2.16	6 700	0.500
	Manduca sexta	29	2.09	50	2.17	6 100	0.500
	Macroglossum stellatarum	73	2.09	21	2.10	2 800	0.500
	Amathes bicolorago	50	2.09	16	1.45	1 600	0.500
	Vespa crabro	104	2.09	24.3	2.64	4 200	0.500
	Vespula vulgaris	143	2.09	13.2	2.75	1 600	0.500
	Bombus terrestris	156	2.60	17.3	2.37	4 500	0.500
	Bombus lapidarius	143	2.60	16.6	2.37	3 700	0.500
	Apis mellifica	240	2.09	10	2.33	1 900	0.500
	Encarsia formosa	400	2.36	0.62	2.70	15	0.577
	Tipula sp.	53	2.09	17.3	3.76	770	0.500
	Theobaldia annulata	262	2.09	6.3	3.94	480	0.500
	Aedes aegypti	600	1.83	2.5	3.57	170	0.500
	Eristalis tenax	182	2.09	12.7	2.65	2 000	0.500
	Calliphora erythrocephala	159	2.09	9.7	2.62	1 000	0.500
Ellington (1984)	Amaxilia fimbriata fluviatilis			58.5	3.90	6 100	0.487
	Ficedula hypoleuca			100	2.21	11 000	0.503
	Manduca sexta			51.8	2.74	5 400	0.499
	Apis mellifica			9.8	3.37	1 600	0.544
	Tipula obsoleta			13.7	5.23	630	0.603
	Eristalis tenax			11.4	3.58	1 600	0.534
	Aeshna juncea			47.4	5.82	1 900	0.567
Ennos (1989)	Tipula paludosa	59	1.95	17	5.24	5 975	0.598
	Bibio marci	99	2.43	11.2	3.34	4 304	0.552
	Conops strigata	144	2.51	7.7	3.95	2 053	0.593
	Eristalis tenax	183	1.50	11.5	3.65	2 399	0.534
	Calliphora vicina	117	2.62	9.2	2.93	3 416	0.540
	Simulium	183	2.60	3.26	2.59	445	0.519
	Drosophila melanogaster	254	2.37	2.02	3.14	142	0.545
Zanker (1990)	Drosophila melanogaster	218	1.22	2.47	2.91	101	0.573

APPENDIX C: POLYNOMIAL MODEL FOR $\overline{C}_L$ PREDICTIONS

Previous studies have shown that the flow structure and the mean lift coefficient of a wing changes with $\mathcal{AR}$, Re, and Ro. Our previous study[32] showed that the effects of $\mathcal{AR}$ on the flow structure can be decoupled using the span-based Reynolds and Rossby numbers, i.e., Re_b and Ro_b, respectively. In that study, predictions of $\overline{C}_L$ were obtained over a three-dimensional parameter space of ranges $1.8 \le \mathcal{AR} \le 7.3$, $75 \le Re_b \le 4000$, and $0.5 \le Ro_b \le 3$, covering those for most insects and wing models in the literature. These data were used to fit a polynomial function P such that

$$\overline{C}_{L(pred)} = P[f(\mathcal{AR}), g(Re_b), h(Ro_b)],$$

Published under license by AIP Publishing

where

$$f(\mathcal{AR}) = \mathcal{AR}, \quad g(Re_b) = \log(Re_b), \quad \text{and} \quad h(Ro_b) = \log(Ro_b). \tag{C1}$$

Here, $f(\mathcal{AR})$, $g(Re_b)$, and $h(Ro_b)$ are the functions of $\mathcal{AR}$, Re_b, and Ro_b, respectively, used to linearize the variables with respect to $\overline{C}_L$. In order to construct the model P, first, a polynomial model of the 4th order is built with all the possible terms in $f(\mathcal{AR})$, $g(Re_b)$, and $h(Ro_b)$ as variables. Furthermore, the LASSO (least absolute shrinkage and selection operator) method is used for the variable selection and regularization. This method helps fitting the data with only selected variables, rather than using all of them. As a result, the polynomial function P reduced to a linear combination of 15 variables with their corresponding coefficients, as shown in Table III.

TABLE III. The polynomial model P was derived as a linear combination of the following terms.

Term	Coefficient
$f(\mathcal{AR})$	−0.020 131
$g(Re_b)$	0.179 068
$h(Ro_b)$	−0.015 914
$g(Re_b)h(Ro_b)$	−0.063 995
$f(\mathcal{AR})g(Re_b)h(Ro_b)$	−0.008 485
$f(\mathcal{AR})[h(Ro_b)]^2$	0.021 444
$[f(\mathcal{AR})]^4$	−0.000 008
$[f(\mathcal{AR})]^3 g(Re_b)$	−0.000 086
$[f(\mathcal{AR})]^3 h(Ro_b)$	0.001 084
$[f(\mathcal{AR})]^2[h(Ro_b)]^2$	0.003 366
$f(\mathcal{AR})[g(Re_b)]^3$	0.000 063
$[g(Re_b)]^4$	−0.000 066
$[g(Re_b)]^2[h(Ro_b)]^2$	−0.003 224
$g(Re_b)[h(Ro_b)]^3$	0.032 481
$[h(Ro_b)]^4$	−0.056 562

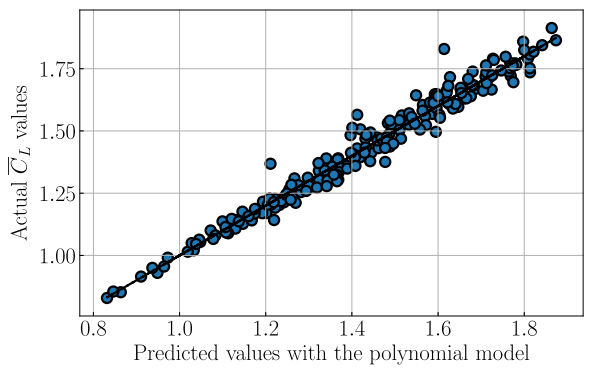

FIG. 17. The comparison of the actual $\overline{C}_L$ values and the predicted values using the polynomial model.

Approximately 100 datapoints were used to fit the model. The comparison of the predictions and the actual values can be seen in Fig. 17. The rms error of this model was 0.604, and the R^2 value of the model was found to be 96.9%. Using a lower-order polynomial resulted in higher rms errors and lower R^2 values. The predictions using the polynomial model followed nearly the same trends, which were expected with the given range of variables, as can be seen in Fig. 14.

REFERENCES

[1] R. Demoll and Hoff, "Der flug der insekten und der vögel," Naturwissenschaften **7**, 480–482 (1919).
[2] M. F. M. Osborne, "Aerodynamics of flapping flight with application to insects," J. Exp. Biol. **28**, 221–245 (1951).
[3] S. Vogel, "Flight in Drosophila: III. Aerodynamic characteristics of fly wings and wing models," J. Exp. Biol. **46**, 431–443 (1967).
[4] T. Weis-Fogh, "Quick estimates of flight fitness in hovering animals, including novel mechanisms for lift production," J. Exp. Biol. **59**, 169–230 (1973).
[5] T. Maxworthy, "Experiments on the Weis-Fogh mechanism of lift generation by insects in hovering flight. Part 1. Dynamics of the 'fling'," J. Fluid Mech. **93**, 47–63 (1979).
[6] C. P. Ellington, "The aerodynamics of hovering insect flight. III. Kinematics," Philos. Trans. R. Soc., B **305**, 41–78 (1984).
[7] M. H. Dickinson, F.-O. Lehmann, and S. P. Sane, "Wing rotation and the aerodynamic basis of insect flight," Science **284**, 1954–1960 (1999).
[8] K. Y. Ma, P. Chirarattananon, S. B. Fuller, and R. J. Wood, "Controlled flight of a biologically inspired, insect-scale robot," Science **340**, 603–607 (2013).
[9] X. Cheng and M. Sun, "Very small insects use novel wing flapping and drag principle to generate the weight-supporting vertical force," J. Fluid Mech. **855**, 646–670 (2018).
[10] J. Han, Z. Yuan, and G. Chen, "Effects of kinematic parameters on three-dimensional flapping wing at low Reynolds number," Phys. Fluids **30**, 081901 (2018).
[11] R. B. R. Azevedo, A. C. James, J. McCabe, and L. Partridge, "Latitudinal variation of wing: Thorax size ratio and wing-aspect ratio in Drosophila melanogaster," Evolution **52**, 1353–1362 (1998).
[12] R. J. Wootton, "Functional morphology of insect wings," Annu. Rev. Entomol. **37**, 113–140 (1992).
[13] J. M. Birch, W. B. Dickson, and M. H. Dickinson, "Force production and flow structure of the leading edge vortex on flapping wings at high and low Reynolds numbers," J. Exp. Biol. **207**, 1063–1072 (2004).
[14] H. Liu and H. Aono, "Size effects on insect hovering aerodynamics: An integrated computational study," Bioinspiration Biomimetics **4**, 015002 (2009).
[15] J. S. Han, J. W. Chang, and S. T. Kim, "Reynolds number dependency of an insect-based flapping wing," Bioinspiration Biomimetics **9**, 046012 (2014).
[16] D. Lentink and M. H. Dickinson, "Rotational accelerations stabilize leading edge vortices on revolving fly wings," J. Exp. Biol. **212**, 2705–2719 (2009).
[17] M. Wolfinger and D. Rockwell, "Flow structure on a rotating wing: Effect of radius of gyration," J. Fluid Mech. **755**, 83–110 (2014).
[18] D. Tudball Smith, D. Rockwell, J. Sheridan, and M. Thompson, "Effect of radius of gyration on a wing rotating at low Reynolds number: A computational study," Phys. Rev. Fluids **2**, 064701 (2017).
[19] T. Jardin and L. David, "Root cutout effects on the aerodynamics of a low-aspect-ratio revolving wing," AIAA J. **55**, 2717–2726 (2017).
[20] R. R. Harbig, J. Sheridan, and M. C. Thompson, "Reynolds number and aspect ratio effects on the leading-edge vortex for rotating insect wing planforms," J. Fluid Mech. **717**, 166–192 (2013).
[21] Y. J. Lee, K. B. Lua, and T. T. Lim, "Aspect ratio effects on revolving wings with Rossby number consideration," Bioinspiration Biomimetics **11**, 056013 (2016).

Published under license by AIP Publishing

[22]J. R. Usherwood and C. P. Ellington, "The aerodynamics of revolving wings II. Propeller force coefficients from mayfly to quail," J. Exp. Biol. **205**, 1565–1576 (2002).
[23]G. Luo and M. Sun, "The effects of corrugation and wing planform on the aerodynamic force production of sweeping model insect wings," Acta Mech. Sin. **21**, 531–541 (2005).
[24]R. R. Harbig, J. Sheridan, M. C. Thompson, C. A. Ozen, and D. Rockwell, "Observations of flow structure changes with aspect ratio for rotating insect wing planforms," AIAA Paper 2012-3282, 2012.
[25]D. J. Garmann and M. R. Visbal, "Dynamics of revolving wings for various aspect ratios," J. Fluid Mech. **748**, 932–956 (2014).
[26]J.-S. Han, J. W. Chang, and H.-K. Cho, "Vortices behavior depending on the aspect ratio of an insect-like flapping wing in hover," Exp. Fluids **56**, 181 (2015).
[27]Z. R. Carr, A. C. DeVoria, and M. J. Ringuette, "Aspect-ratio effects on rotating wings: Circulation and forces," J. Fluid Mech. **767**, 497–525 (2015).
[28]N. Phillips, K. Knowles, and R. J. Bomphrey, "The effect of aspect ratio on the leading-edge vortex over an insect-like flapping wing," Bioinspiration Biomimetics **10**, 056020 (2015).
[29]J. W. Kruyt, G. F. van Heijst, D. L. Altshuler, and D. Lentink, "Power reduction and the radial limit of stall delay in revolving wings of different aspect ratio," J. R. Soc., Interface **12**, 20150051 (2015).
[30]A. Shahzad, F.-B. Tian, J. Young, and J. C. S. Lai, "Effects of wing shape, aspect ratio and deviation angle on aerodynamic performance of flapping wings in hover," Phys. Fluids **28**, 111901 (2016).
[31]T. Jardin and T. Colonius, "On the lift-optimal aspect ratio of a revolving wing at low Reynolds number," J. R. Soc., Interface **15**, 20170933 (2018).
[32]S. S. Bhat, J. Zhao, J. Sheridan, K. Hourigan, and M. C. Thompson, "Uncoupling the effects of aspect ratio, Reynolds number and Rossby number on a rotating insect-wing planform," J. Fluid Mech. **859**, 921–948 (2019).
[33]S. A. Ansari, K. Knowles, and R. Zbikowski, "Insectlike flapping wings in the hover. Part II: Effect of wing geometry," J. Aircr. **45**, 1976–1990 (2008).
[34]D. Wang, J. Wu, and Y. Zhang, "Effects of geometric parameters on flapping rotary wings at low Reynolds numbers," AIAA J. **56**, 1372–1387 (2018).
[35]C. P. Ellington, "The aerodynamics of hovering insect flight. II. Morphological parameters," Philos. Trans. R. Soc., B **305**, 17–40 (1984).
[36]X. G. Meng and M. Sun, "Aerodynamics and vortical structures in hovering fruitflies," Phys. Fluids **27**, 031901 (2015).
[37]M. Wolf, L. C. Johansson, R. von Busse, Y. Winter, and A. Hedenström, "Kinematics of flight and the relationship to the vortex wake of a Pallas' long tongued bat (*Glossophaga soricina*)," J. Exp. Biol. **213**, 2142–2153 (2010).
[38]S. Wang, X. Zhang, G. He, and T. Liu, "Lift enhancement by dynamically changing wingspan in forward flapping flight," Phys. Fluids **26**, 061903 (2014).
[39]S. Wang, X. Zhang, G. He, and T. Liu, "Lift enhancement by bats' dynamically changing wingspan," J. R. Soc., Interface **12**, 20150821 (2015).
[40]H. Tennekes, *The Simple Science of Flight: From Insects to Jumbo Jets* (MIT Press, 2009).
[41]A. R. Ennos, "The effect of size on the optimal shapes of gliding insects and seeds," J. Zool. **219**, 61–69 (1989).
[42]C. H. Greenewalt, "The wings of insects and birds as mechanical oscillators," Proc. Am. Philos. Soc. **104**, 605–611 (1960).
[43]J. M. Wakeling and C. P. Ellington, "Dragonfly flight II. Velocities, accelerations and kinematics of flapping flight," J. Exp. Biol. **582**, 557–582 (1997).
[44]A. Cespedes, C. M. Penz, and P. J. DeVries, "Cruising the rain forest floor: Butterfly wing shape evolution and gliding in ground effect," J. Anim. Ecol. **84**, 808–816 (2015).
[45]G. R. Spedding, "The aerodynamics of flight," in *Mechanics of Animal Locomotion*, Advances in Comparative and Environmental Physiology, 1st ed. (Springer-Verlag Berlin Heidelberg, 1992), Chap. 3, pp. 51–111.
[46]J. M. Zanker, "The wing beat of Drosophila melanogaster. I. Kinematics," Philos. Trans. R. Soc., B **327**, 1–18 (1990).
[47]S. A. Combes and T. L. Daniel, "Flexural stiffness in insect wings I. Scaling and the influence of wing venation," J. Exp. Biol. **206**, 2979–2987 (2003).
[48]D. Lentink and M. H. Dickinson, "Biofluiddynamic scaling of flapping, spinning and translating fins and wings," J. Exp. Biol. **212**, 2691–2704 (2009).
[49]T. Jardin and L. David, "Coriolis effects enhance lift on revolving wings," Phys. Rev. E **91**, 031001(R) (2015).
[50]J. D. Eldredge and A. R. Jones, "Leading-edge vortices: Mechanics and modeling," Annu. Rev. Fluid Mech. **51**, 75–104 (2019).
[51]C. P. Ellington, C. van den Berg, A. P. Willmott, and A. L. R. Thomas, "Leading-edge vortices in insect flight," Nature **384**, 626–630 (1996).
[52]I. Borazjani and M. Daghooghi, "The fish tail motion forms an attached leading edge vortex," Proc. R. Soc. B **280**, 20122071 (2013).
[53]R. G. Bottom, I. Borazjani, E. L. Blevins, and G. V. Lauder, "Hydrodynamics of swimming in stingrays: Numerical simulations and the role of the leading-edge vortex," J. Fluid Mech. **788**, 407–443 (2016).
[54]E. Limacher, C. Morton, and D. Wood, "On the trajectory of leading-edge vortices under the influence of Coriolis acceleration," J. Fluid Mech. **800**, R1-1–R1-14 (2016).
[55]T. Jardin, "Coriolis effect and the attachment of the leading edge vortex," J. Fluid Mech. **820**, 312–340 (2017).
[56]Y. Lu, G. X. Shen, and G. J. Lai, "Dual leading-edge vortices on flapping wings," J. Exp. Biol. **209**, 5005–5016 (2006).
[57]A. R. Jones, A. Medina, H. Spooner, and K. Mulleners, "Characterizing a burst leading-edge vortex on a rotating flat plate wing," Exp. Fluids **57**, 52 (2016).
[58]S. A. Ansari, K. Knowles, and R. Zbikowski, "Insectlike flapping wings in the hover. Part I: Effect of wing kinematics," J. Aircr. **45**, 1945–1954 (2008).
[59]S. S. Bhat, J. Zhao, J. Sheridan, K. Hourigan, and M. C. Thompson, "Evolutionary shape optimisation enhances the lift coefficient of rotating wing geometries," J. Fluid Mech. **868**, 369–384 (2019).
[60]S. S. Bhat, J. Zhao, J. Sheridan, K. Hourigan, and M. C. Thompson, "The leading-edge vortex on a rotating wing changes markedly beyond a certain central body size," R. Soc. Open Sci. **5**, 172197 (2018).
[61]W. B. Dickson and M. H. Dickinson, "The effect of advance ratio on the aerodynamics of revolving wings," J. Exp. Biol. **207**, 4269–4281 (2004).
[62]R. R. Harbig, J. Sheridan, and M. C. Thompson, "The role of advance ratio and aspect ratio in determining leading-edge vortex stability for flapping flight," J. Fluid Mech. **751**, 71–105 (2014).
[63]A. Shahzad, F.-B. Tian, J. Young, and J. C. S. Lai, "Effects of Hawkmoth-like flexibility on the aerodynamic performance of flapping wings with different shapes and aspect ratios," Phys. Fluids **30**, 091902 (2018).
[64]Y. Z. Lyu, H. J. Zhu, and M. Sun, "Aerodynamic forces and vortical structures of a flapping wing at very low Reynolds numbers," Phys. Fluids **31**, 041901 (2019).
[65]S. P. Sane and M. H. Dickinson, "The control of flight force by a flapping wing: Lift and drag production," J. Exp. Biol. **204**, 2607–2626 (2001).
[66]A. R. Ennos, "The kinematics and aerodynamics of the free flight of some diptera," J. Exp. Biol. **142**, 49–85 (1989).

Published under license by AIP Publishing